Basin Research
IAS EAGE

# A model for underpressure development in a glacial valley, an example from Adventdalen, Svalbard



| | |
|---|---|
| Journal: | *Basin Research* |
| Manuscript ID: | BRE-080-2014.R3 |
| Manuscript Type: | Original Article |
| Date Submitted by the Author: | 30-Mar-2015 |
| Complete List of Authors: | Wangen, Magnus; Institute for Energy Technology, Energy and Environment<br>Souche, Alban; Institute for Energy Technology, Energy and Environment<br>Johansen, Harald; Institute for Energy Technology, Energy and Environment |
| Keywords: | modelling, tectonic geomorphology, basin fluids |
| | |

# A model for underpressure development in a glacial valley, an example from Adventdalen, Svalbard

Magnus Wangen [1*], Alban Souche [1], Harald Johansen [1]

*(1) Institute for Energy Technology, P.O.Box 40, N-2027 Kjeller, Norway*

*(* ) Corresponding author. E-mail: Magnus.Wangen@ife.no, tel: +47-4767-9534, fax: +47-6381-5553*

January 2015

**Abstract**

The underpressure observed in the glacial valley Adventdalen at Svalbard is studied numerically with a basin model and analytically with a compartment model. The pressure equation used in the basin model, which accounts for underpressure generation, is derived from mass conservation of pore fluid and solid, in addition to constitutive equations. The compartment model is derived as a similar pressure equation, which is based on a simplified representation of the basin geometry. It is used to derived analytical expressions for the underpressure (overpressure) from a series of unloading (loading) intervals. The compartment model gives a characteristic time for underpressure generation of each interval, which tells when the pressure state is transient or stationary. The transient pressure is linear in time for short time spans compared to the characteristic time, and then it is proportional to the weight removed from the surface. We compare different contributions to the underpressure generation and find that porosity rebound from unloading is more important than the decompression of the pore fluid during unloading and the the thermal contraction of the pore fluid during cooling of the subsurface. Our modelling shows that the unloading from the last deglaciation can explain the present day underpressure. The basin model simulates the subsurface pressure resulting from erosion and unloading in addition to the fluid flow driven by the topography. Basin modelling indicates that the mountains surrounding the valley are more important for the topographic driven flow in the aquifer than the recharging in the neighbour valley. The compartment model turns out be useful to estimate the orders of magnitude for system properties like seal and aquifer permeabilities and decompaction coefficients, despite its geometric simplicity. We estimate that the DeGeerdalen aquifer cannot have a permeability that is higher than $1 \cdot 10^{-18}$ $m^2$, since otherwise, the fluid flow in the aquifer becomes dominated by topographic driven flow. The upper value for the seal permeability is estimated to be $1 \cdot 10^{-20}$ $m^2$, since higher values preclude the generation and preservation of underpressure. The porosity rebound is estimated to be less than $0.1$ % during the last deglaciation using a decompaction coefficient $\alpha_r = 1 \cdot 10^{-9}$ $Pa^{-1}$.

**Keywords:** unloading, erosion, underpressure, fracture porosity.

# 1 Introduction

Pore fluid pressure below the hydrostatic pressure is not so common in sedimentary basins. The common situation is hydrostatic pressure or overpressure. Underpressure was discovered during the drilling of test well DH4 in Adventdalen at Svalbard, see figure 1. The well DH4 showed $:40$ bar pressure at 870 m depth in the DeGeerdalen formation (fm), which is an interbedded layer of sandstone and silty-sandstones [Braathen et al. , 2012]. DeGeerdalen fm is of Triassic age, and it is buried underneath a $:500$ m thick layer of shales and siltstones from the Jurassic and the Cretaceous. The well is situated at the base of a valley where there is a little more than 100 m of permafrost. The valley Adventdalen was carved out during the Pliocene and Pleistocene ice-ages. The glacial erosion and the rapid last deglaciation have unloaded the brittle Mesozoic sediments in the subsurface of the valley.

There are several studies of underpressure generation in similar settings. [Corbet Bethke, 1992, Bachu Underschultz, 1995, Parks Toth, 1995, Bekele et al. , 2003] have examined causes for the underpressure in the Alberta basin, and they have all linked it to unloading by erosion or deglaciation. [Bekele et al. , 2003] found that underpressure is caused mainly by deglaciation, because Pliocene to recent erosion rates were too slow. They used basin modelling software to simulate the underpressure. [Lazear, 2009] relates the underpressure in the Piceance basin in West-Central Colorado to regional uplift and a 1.5 km incision, where 0.1% fracture porosity is estimated from the unloading. [Vinard et al. , 2001] modelled the underpressure at Wellenberg site in Switzerland with different scenarios of erosion and unloading using the software ABAQUS with a poro-elastic rheology. They concluded that unloading from deglaciation gives results that best fit the observations. Several other studies have also linked underpressure in reservoir units to uplift, erosion and unloading when the reservoir unit is vertically sealed from the surface [Russell, 1972, Bradley, 1975, Chapman, 1976, Dickey Cox, 1977, Neuzil Pollock, 1983]. A common explanation for the underpressure is porosity rebound from the unloading [Neuzil Pollock, 1983, Corbet Bethke, 1992, Luo Vasseur, 1995]. A hypothesis that has received less support is the thermal contraction of a cooling pore fluid when it is brought towards the surface during erosion [Russell, 1972, Bradley, 1975, Lou Vasseur, 1992, Hall, 1994, Swarbrick Osborne, 1997]. It should also be mentioned that topographic driven flow creates underpressure underneath the locally highest areas, where the flow field is vertically downwards [Toth, 1978, Orr Kreitler, 1985]. A number of authors have modeled regional scale groundwater flow systems driven by glaciation [Belitz Bredehoeft, 1988, Lemieux et al. , 2008a, Lemieux et al. , 2008c, Lemieux et al. , 2008b, Bense Person, 2008, Iverson Person, 2012], but these studies are less directed towards underpressure generation.

Adventdalen valley has undergone a complex geohistory with glacial erosion and several tens of cycles of glaciation during the last 3.5 Ma, involving rapid deglaciations [Starkel, 2003, Eiriksson, 2008, Geirsd_ttir, 2011]. The underpressure is therefore linked with a series of different episodes of unloading/loading, combined with an uncertain rheology of fractured rocks. This study looks at ways to quantify the underpressure in the DeGeerdalen formation, when it is generated by unloading. We aim at estimating the megascopic permeabilities of the underpressured aquifer and the seal, and to estimate the amount of pore space expansion that

is necessary for the generation of the observed underpressure. These properties are estimated when accounting for the different time-intervals of unloading. The rocks in DH4 are fractured and it could be that most of the void space produced by unloading is due to reopening of joints and fractures by reduction in the vertical effective stress.

We have developed a compartment model for the underpressure generation, which is a pressure equation based on a simplified representation of the geometry of the basin. The simplified geometry allows us to produce analytical expressions for the underpressure, which are otherwise difficult to obtain. A similar modelling approach has earlier been used to study the generation and dissipation of overpressure in fault bounded compartments in reservoir formations [Borge, 2002]. The analytical results from the compartment model are used to derive a condition for underpressure generation that is similar to a condition for overpressure generation in basins during sediment deposition and burial.

Even though the basin geometry is simplified in the compartment model, it has the same sink term that generates underpressure as the basin model. This sink (or source) term has contributions to the underpressure from porosity rebound, thermal contraction of the fluid and decompression of the fluid. We compare these contributions to find the process that dominates underpressure generation.

The compartment model includes a term for topographic driven flow, which is represented by a potential for recharging the aquifer. It is possible that the aquifer is recharged from the neighbouring valley, where the DeGeerdalen formation is exhumed at a height 200 m above the surface of Adventdalen. On the other hand, the mountains surrounding the valley also drive fluid flow, which can be important for the underpressure in the DeGeerdalen formation. The 2D basin model is needed to study the nature of the topographic driven flow in Adventdalen.

This paper is organized as follows: The underpressure observations are first presented, then observations of glaciations in Adventdalen, before the surface sediment temperatures are commented. The compartment model is introduced, and its transient- and stationary states are analyzed. The different contributions to the source/sink term in the equation for underpressure are compared. The compartment model is then applied to cycles of glacial loading and unloading, before it is applied to different scenarios for underpressure generation in Adventdalen. Finally, results of basin modelling of Adventdalen are presented.

The technical parts of modelling are collected in the Appendices. The pressure equation for underpressure generation and fluid flow is derived in Appendix A, from mass conservation of the fluid and solid. The rheology of porosity rebound from unloaded sediments is presented in Appendix B, the pressure equation of the compartment model is derived in Appendix C and the condition for stationary underpressure is presented in Appendix D.

## 2 Geological observations

## 2.1 Underpressure in DeGeerdalen formation

The well DH4 was drilled in Adventdalen down to 970 m to test if the Triassic reservoir formations in DeGeerdalen (fm) could be a suitable reservoir for CO2 storage. Figure 2 gives the lithostratigraphy of DH4, where DeGeerdalen appears as sandstones interbedded with siltstones. [Braathen et al. , 2012] give a comprehensive review of the data collected for well DH4. Well testing by water injection showed a water level that was substantially below the hydrostatic pressure relative to the valley surface. [Braathen et al. , 2012] report that well DH4 has a $:40$ bar pressure at 870 m depth in the DeGeerdalen formation (fm), a fluid pressure that is 47 bar below the 87 bar hydrostatic pressure. The interbedding of sandstones with siltstone divides DeGeerdalen into subunits with possibly different underpressures.

Sandstone porosities were measured in the range from 5% and 20% in well DH4, and laboratory measurements on core-plugs indicate that the majority of analysed sandstone units have permeabilities in the range from 0.01 mD to 1 mD [Braathen et al. , 2012]. The well testing was carried out for reservoir units in the depth interval of 870 m to 970 m. The average permeability of the reservoir rock was estimated to 45 mD over the sandstone intervals, based on the well testing. This permeability is between one and two orders of magnitude above the largest values measured for the core permeabilities. The discrepancy is explained as fracture permeability resulting from the well testing. The well pressure indicated that hydraulic fracturing took place during fluid injection.

Some of the rock units in the depth interval 440 m to 705 m appear to be highly fractured [Ogata et al. , 2012]. A least 284 fractures were observed in this interval with acoustic televiewer and 97% of the fractures were subhorizontal. The siltstones in the caprock appear to be fractured, too. The presence of fractures in DH4 is most likely important for rock properties like porosity, permeability and the decompaction coefficient. The fracture porosity may create the void space responsible for underpressure. A fractured rock may also more easily decompact during unloading, which implies a larger decompaction coefficient for fractured rock than for intack rock. Although the rocks in the DH4 are fractured the difference in pressure indicates isolated pressure compartments in the rock succession.

The permafrost in DH4 is measured to be in the range from 120 m to 160 m [Braathen et al. , 2012], and below the permafrost there is a slightly overpressured aquifer. The reservoir intervals of the DeGeerdalen formation are separated from the shallow aquifer by a seal of approximately 500 m of siltstone (see figure 2). Janusfjellet Subgroup is a low permeable seal even though it is a highly fractured cap rock. The fractures must be closed in the seal, because the seal is clearly separating the underpressured reservoir rocks from the near hydrostatic aquifer underneath the permafrost [Ogata et al. , 2012].

## 2.2 Glaciations in Adventdalen

Adventdalen has gone through a long period of slow unloading from glacial erosion during the Pliocene and Pleistocene. The valley, which is approximately 1000 m deep, was carved out during this period. In the same period there were several tens of episodes of glaciation interrupted by shorter and warm interglacial periods. The periods of glaciations and deglaciations produce fluctuations in the decreasing load from the erosion of the valley. Mapping of glacial deposits found within the basaltic lava flows of Iceland has revealed at least 22 glacial-interglacial cycles during the last 3.5 Ma [Geirsd_ttir, 2011]. The last deglaciation was rapid compared with the build-up of the ice [Starkel, 2003]. The rapid climatic change at the Younger Dryas-Preboreal transition is well documented in a variety of settings as for instance the fluvial environment of Polish rivers [Starkel, 2003]. [Paus, 1989] reports that the first vegetational responses of the warmer climate in the Holocene in SW Norway is around 10.5 ka and that dense forests develop around 10 ka. At Svalbard during the period 11.5 - 10.6 ka BP the fauna indicates increased influence of Atlantic Water and the final deglaciation of the fjord after the Younger Dryas period [Skirbekk et al. , 2010].

### 2.3 The sediment surface temperature under the ice

The underpressure compartment becomes colder during an erosion process, as it moves upwards towards the sediment surface. The cooling can be approximated assuming a stationary geotherm, which is a reasonable assumption as long as the temperature at the sediment surface does not vary much. This is the case for wet based glaciers and also for parts of polythermal glacier, where the temperature at the base is close to the pressure-melting point. A wet-based glacier is close to the pressure-melting point everywhere in its interior, as opposed to a cold-based (polar) glacier, where the temperature is everywhere below the pressure-melting point. Cold-based glaciers are frozen to their beds and move slowly by internal deformation. An intermediate polythermal glacier is at the pressure-melting point at the base, but not necessarily throughout the entire glacier [Sharp, 1988, Hambrey Glasser, 2012, L uthi Funk, 2013]. The temperature is slightly below 0 $^\circ$C at the pressure-melting point for a large range of glacier thicknesses [L uthi Funk, 2013]. In the following we assume that the base of ice in the valley has the temperature 0 $^\circ$C.

## 3 A compartment model of underpressure generation

The basic behaviour of the underpressure development in the DeGeerdalen (fm) can be addressed by means of a model for just the pressure in the reservoir compartment. A sketch of the model is shown in figure 3. Conservation of fluid mass for the compartment can be expressed by the pressure equation

$$t_0 \frac{dp}{dt} + p = p_s, \tag{1}$$

as shown in Appendix C, where $p$ is the unknown compartment underpressure, $t_0$ is the characteristic time for pressure transients and $p_s$ is the stationary underpressure. The underpressure is defined as fluid pressure minus the hydrostatic pressure. The characteristic time is

$$t_0 = \frac{\phi \alpha_{\text{eff}} \mu}{N_s + N_a} \tag{2}$$

where $\phi$ is the porosity, $\alpha_{\text{eff}}$ is the effective compressibility of the system and $\mu$ is the fluid viscosity. The two dimensionless numbers in the denominator are

$$N_a = \frac{k_a}{l_1 l_2}, \qquad and \qquad N_s = \frac{k_s}{h_1 h_2} \tag{3}$$

where $k_a$ and $k_s$ are the aquifer permeability and seal permeability, respectively. The model does not account for lateral variations in the permeability fields. The main permeability variation is the strong contrast between the seal and the aquifer permeabilities. The thickness of the sealing layer is $h_1$ and the thickness of the reservoir compartment is $h_2$. The aquifer extends a distance $l_1$ to the left and the width of the compartment is $l_2$. The two dimensionless numbers $N_a$ and $N_s$ control the flow properties of the aquifer and the seal, respectively. We will see that the permeabilities always appear together with distance or thickness as expressed by these numbers. There is a characteristic time $t_s = \phi \alpha_{\text{eff}} \mu / N_s$ for the vertical version of the model, when $N_a = 0$, and lateral flow in the aquifer is unimportant. Correspondingly, there is a characteristic time $t_a = \phi \alpha_{\text{eff}} \mu / N_a$ for the lateral version of the model, when $N_s = 0$, and flow vertically through the seal is unimportant. We also notice that the characteristic time of the system is half the harmonic average of the two subsystems, $t_0 = t_a t_s / (t_a + t_s)$. Appendix C shows how the characteristic time $t_0$ controls the decay of the initial pressure and how it controls the transient towards a new stationary state.

The stationary underpressure can be split into the sum of two contributions as

$$p_s = p_\omega + p_m \tag{4}$$

where

$$p_\omega = \frac{\phi \mu}{N_s + N_a} \left( \alpha_{\text{eff}} \rho_f g \omega_u - \beta \frac{dT}{dz} \omega - \frac{\alpha_r \rho_b g \omega}{(1-\phi)} \right) \tag{5}$$

is the stationary underpressure from unloading, while

$$p_m = (\frac{N_a}{N_s + N_a}) p_1 \tag{6}$$

is the stationary overpressure contribution from the topographic potential $p_1$. The stationary pressure introduses the following parameters: $\rho_b$ is the bulk density, $\rho_f$ is the brine density, $\beta$ is the thermal expansibility, $dT/dz$ is the thermal gradient, $\omega$ is the erosion rate, $\omega_u$ is the uplift rate and $g$ is the constant of gravity (see Appendix B). The overpressure contribution from topographic driven flow becomes negligible in the regime where $N_s >> N_a$ and the contribution is at maximum for the opposite regime $N_s << N_a$. The potential $p_1$ and the number $N_a$ may be viewed in a broader sense than in the figure 3. The potential $p_m$ can represent any topographic flow that affects the compartment. For example, the parameters that make $p_m$ can be calibrated to represent the recharge of the aquifer from both sides of a system that is symmetric around the center of the valley, or to represent the topographic flow from one or both mountains surrounding the valley.

The stationary underpressure (5) is the sum of three terms, the first term is the contribution from decompaction, the second term is underpressure generation from thermal contraction of the fluid as the compartment moves upwards along the geotherm $T(z)$ during erosion, and the third term is overpressure generation due to the decompression of the fluid. These three contributions to the underpressure are compared in section 3.2.

The stationary pressure (5), which is a part of the sink term in the compartment model, has a similar form as the sink term in the full pressure equation (17) (see Appendix A). The main difference between the sink terms is that the compartment model has an explicit representation of the geometry through the numbers $N_a$ and $N_s$, and the overpressure from topographic driven flow.

## 3.1 The transient state and the stationary state

The case of short unloading compared to the characteristic time $t_0$ is of special interest. Assuming that duration of the unloading is short, $t = t_0$, yields

$$p(t) \approx p_s \frac{t}{t_0} \tag{7}$$

when the initial pressure is zero. In this regime underpressure generation is proportional to the duration of the unloading and the final stationary underpressure. We will later recognize this linear pressure response when unloading is rapid, for instance deglaciation. The underpressure

increment becomes

$$\Delta p \approx \frac{\alpha_r}{\alpha_{\text{eff}}} \rho_b g h \tag{8}$$

where the $h$ is the thickness of the eroded section and $\alpha_r$ is the decompaction coefficient, when decompaction dominates thermal expansion and fluid decompression. An important observation is that a time span much shorter than the characteristic time ($t << t_0$) generates underpressure that does not depend on permeabilities, only on the compressibilities and the load that is removed. If the decompaction coefficient is much larger than the fluid compressibility ($\alpha_r >> \alpha_{\text{f}}$) the estimate (8) simplifies to $\Delta p \approx \rho_b g h$.

It is instructive to see what the porosity rebound is for the initial transient regime and for the stationary regime. The porosity rebound is given by (30), and inserting the transient underpressure (7) yields

$$\Delta\phi = \phi\alpha_r(1-\frac{\alpha_r}{\alpha_{\text{eff}}})\rho_b g\omega t, \qquad t << t_0 \tag{9}$$

It is assumed that erosion takes place without uplift ($\omega_u = 0$) and that there is no topographic driven fluid flow. The rebound during the stationary state under the same conditions yields

$$\Delta\phi = \phi\alpha_r(t-\frac{\alpha_r}{\alpha_{\text{eff}}}t_0)\rho_b g\omega, \qquad t >> t_0 \tag{10}$$

The porosity rebound is in both cases, $t << t_0$ and $t >> t_0$, linear in time. The rebound compressibility is less than the effective compressibility, $\alpha_r/\alpha_{\text{eff}} < 1$, which produces a positive porosity increment for both cases. An observation is that the porosity rebound becomes independent of the seal permeability in the limit $t << t_0$ and weakly dependent on the seal permeability in the opposite regime, $t >> t_0$.

## 3.2 Thermal contraction and decompaction compared with fluid decompression

The stationary underpressure from unloading, expression (5), has three terms that represents three different processes. The first term is underpressure from porosity rebound, the second is underpressure from thermal contraction of the fluid as it moves upwards along a geotherm, and the third term is an overpressure contribution from decompression of the fluid. We will now compare these terms. First we compare thermal expansion against decompression of the fluid when uplift and erosion take place at the same rate, and we get

$$\frac{thermal\ expansion}{decompression} = \frac{\beta dT/dz}{\alpha_{\text{eff}}\rho_f g} = 0.9 \tag{11}$$

using that $\beta = 2\cdot10^{-4}$ [1/K], $dT/dz = 0.045$ [C/m], $\alpha_{\text{f}} = \alpha_r = 5\cdot10^{-10}\ \ Pa^{-1}$, $\rho_f = 1000\ \ kg\ m^{-3}$ and $g = 10$ m/s$^2$. The thermal gradient is an average for the well DH4 [Elvebakk, 2010], the thermal expansion coefficient is for water at 20 $^\circ$C [Liley Gambill, 1973] and the compressibility is for water at 20 $^\circ$C and 13 MPa [Liley Gambill, 1973]. The effect of the thermal contraction of the water for the thermal gradient of Adventdalen is seen to be almost equally important as decompression, when the decompression coefficient is equal to the compressibility of water.

The overpressure generation from decompression of water can also be compared with underpressure created by porosity rebound (decompaction), as expressed by the coefficient $\alpha_r$ in equation (5). We get that

$$\frac{decompaction}{decompression} = \frac{\alpha_r\rho_b}{(1-\phi)\alpha_{\text{eff}}\rho_f} \approx \frac{\alpha_r\rho_b}{(\alpha_{\text{f}}+\alpha_r)\rho_f} = 1.25 \tag{12}$$

when $\alpha_r = \alpha_{\text{f}} = 5\cdot10^{-10}\ \ Pa^{-1}$, $\rho_f = 2500\ \ kg\ m^{-3}$, $\rho_f = 1000\ \ kg\ m^{-3}$ and $\phi = 0.1$. The two ratios (11) and (12) show that thermal contraction along the geotherm at Adventdalen has roughly the same effect as porosity expansion when $\alpha_r = \alpha_{\text{f}}$.

## 3.3 Repeated cycles of glaciation and deglaciation

There have been several tens of glacial periods with short interglacials [Geirsdottir, 2011]. The glacials last typically 100 ka while the interglacials are much shorter, a few thousand years [Petit et al. , 1999]. The glacier-interglacier cycles may be modelled with equation (33) where one cycle consists of glaciation over $\Delta t_a = 100$ ka and then deglaciation over $\Delta t_b = 1$ ka. The glacier grows steadily in thickness until its maximum at the end of glaciation, and then melts down steadily during the interval of deglaciation. The pressure at the end of one time-interval becomes the initial condition for the next interval in the expression for compartment pressure, see equations (35) and (36) in Appendix C.

The stationary pressure values that enter the solution are based on the rates of loading and unloading $\omega_a = -\Delta h/\Delta t_a$ and $\omega_b = \Delta h/\Delta t_b$, respectively, where $\Delta h$ is the thickness of the ice. The minus sign is explicitly added to $\omega_a$ to assure that it is loading and therefore generates overpressure. The loading/unloading rates go into into the stationary pressure $p_s$ given by equation (5), which again is used in the transient pressure solutions (35) and (36).

The pressure fluctuations during several cycles of glaciation-deglaciation are shown in figure 4. The time of each interval is scaled to the unit interval, which means that each cycle covers two

units on the x-axis. The case of figure 4a has a aquifer permeability $k_a = 5 \cdot 10^{-18}\ m^2$, a seal permeability $k_s = 1 \cdot 10^{-20}\ m^2$ and the decompaction/compaction coefficient $\alpha_r = 1 \cdot 10^{-9}\ Pa^{-1}$. The same coefficient $\alpha_r$ is used for compaction during glacial loading as for deglacial unloading. The dimensionless time-intervals are $\tau_a = 5.2$ and $\tau_b = 0.05$. Glaciation spans a time interval that is much longer than the characteristic time of the system ($t_0$). We can see that from figure 4a, because the pressure build-up approaches the stationary value $p_{s,a} = p_{\omega,a}$. The stationary value $p_{s,a} = p_{\omega,a}$ will be researched when the curve becomes flat. The time interval of deglaciation is much shorter than $t_0$, because the pressure decrease is linear during deglaciation, which is clearly a transient phase. The transient is also far from reaching its stationary value $p_{s,b} = p_{\omega,b}$, because the curve is far away from flattening out.

Figure 4b shows the case with the reduced permeabilities, $k_a = 1 \cdot 10^{-19}\ m^2$ and $k_s = 1 \cdot 10^{-21}\ m^2$. The seal permeability is reduced by one order of magnitude, which makes the characteristic time of the system nearly one order of magnitude larger. The dimensionless interval lengths become $\tau_a = 0.26$ and $\tau_b = 0.0026$, and both phases become transient with linear pressure response.

The initial pressure before the cycles start is 0 bar and after a few cycles the pressure oscillates between two fixed values. The upper and lower pressure values for the oscillations can be obtained as stationary initial conditions as shown in Appendix C. The case where both time intervals are much longer than the characteristic time ($\tau_a >> 1$ and $\tau_b >> 1$) produces $p_1 \approx p_{s,a}$ and $p_2 \approx p_{s,b}$, which are the stationary values for the two intervals, respectively. The more likely case where $\tau_a >> 1$ and $\tau_b << 1$ (see figure 4a) produces $p_1 \approx p_{s,a}$ which is the stationary pressure for the interval, and $p_2 \approx p_{s,b} + (p_{s,a} - p_{s,b})\exp(-\tau_b)$ which is the pressure predicted by the equation (33).

The pressure evolution in figure 4a, where $\tau_a >> 1$ and $\tau_b << 1$, is reasonable for Adventdalen. A period of 100 ka of glacial loading therefore leads to a small stationary overpressure, and the short interval of deglaciation leads to a noticeable underpressure. Therefore, we ignore the oscillations in glacial loading before the last glaciation. It should be noted that the glacial periods are far from regular and that they are superposed by large fluctuations of warmer and colder climate [Petit et al. , 1999].

## 4 The compartment model applied to Adventdalen

## 4.1 Three stages of underpressure generation

We simplify the glacial past (see section 2.2) by dividing it into three intervals of unloading - first is the long and slow glacial erosion over a time span of $\Delta t_1 = 3.5$ Ma, then a short and rapid deglaciation over a period of $\Delta t_2 = 1$ ka and finally a period of rest $\Delta t_3 = 10$ ka, from the end of last deglaciation until today. The cyclic fluctuations in the ice thickness and thereby the ice load is ignored during the first interval of glacial erosion.

An important parameter in the stationary pressure for each time interval $\Delta t_i$ ($i = 1,2,3$) is the erosion (or deglaciation) rate $\omega_i$. The altitude of the mountains surrounding Adventdalen is roughly 1000 m, which indicates that the present day U-valleys were eroded by the main glaciers from a plateau that was at least $\Delta h_1 = 1000$ m above sea level. The erosion rate during period $\Delta t_1$ is therefore taken to be $\omega_1 = \Delta h_1 / \Delta t_1 = 286$ m/Ma. For simplicity, we take the uplift rate to be zero.

The ice filled the valley with roughly $\Delta h_2 = 400$ m, which makes the rate of deglaciation $\omega_2 = \Delta h_2 / \Delta t_2$ m/a = $0.4$ m/a. The assumption of a temperature close to 0 $^\circ$C at the base of the ice during the period deglaciation implies that there is no temperature change in the underpressure compartment during this time interval. There is no permafrost underneath those parts of the glaciers that have a temperature close to 0 $^\circ$C [Sharp, 1988]. Therefore, it is no thermal contraction of the fluid during the unloading, only decompaction and porosity rebound.

Once the glacier has melted the surface becomes exposed to a climate with an annual mean temperature below 0 $^\circ$C and permafrost starts to grow from the surface. The annual mean temperature in Adventdalen is today $-5$ $^\circ$C. Temperature measurements in well DH4 suggest that the mean could have been even lower, may be down to $-8$ $^\circ$C in the recent past [Elvebakk, 2010]. The growth of the permafrost was a transient thermal effect that took place after the deglaciation. Today, the permafrost in Adventdalen is in the range from 120 m to 160 m in DH4 [Braathen et al. , 2012]. Therefore, the recent cooling of the pressure compartment might be important for underpressure generation. There is no pressure generation from unloading during this last time interval, only form thermal contraction. The thermal contraction can be handled with the compartment model by letting the reduction of the temperature $\Delta T$ take place at the rate $\Delta T / \Delta t_3 = (dT/dz)\omega$. The three different stages of the compartment is summarized in table 1.

## 4.2 The present day underpressure after three stages of unloading

The underpressure after three stages of unloading can be computed with the expression (34) from Appendix C, which includes the potential from topographic driven fluid. Figure 5 demonstrates the computation of the present day underpressure using equation (34). The

parameters for the underpressure compartment at Adventdalen are collected in table 2. The aquifer permeability is varied from over 5 orders of magnitude from $k_a = 1 \cdot 10^{-20}$ $m^2$ to $k_a = 1 \cdot 10^{-15}$ $m^2$ and the seal permeability is also varied over 5 orders of magnitude from $k_s = 1 \cdot 10^{-23}$ $m^2$ to $k_s = 1 \cdot 10^{-18}$ $m^2$. Figure 5a has the decompaction coefficient $\alpha_r = 1 \cdot 10^{-10}$ $Pa^{-1}$, which is $1/5$ of the compressibility of water. The water compressibility therefore dominates this case. Present day underpressure in the range of $40$ bar is not possible unless the aquifer permeability is less than $1 \cdot 10^{-19}$ $m^2$ and the seal permeability is less than $1 \cdot 10^{-21}$ $m^2$, which is a low permeable system. Increasing the decompaction coefficient with one order of magnitude to $\alpha_r = 1 \cdot 10^{-9}$ $Pa^{-1}$ makes it twice as large as the water compressibility. But the upper limits of the permeabilities increase less than a factor 10, as seen from figure 5b. The system still has to have low permeability to allow for the present day underpressure. Increasing the decompaction coefficient to 20 times the water compressibility allows for an aquifer permeability larger than $1 \cdot 10^{-18}$ $m^2$ and a seal permeability larger than $1 \cdot 10^{-20}$ $m^2$.

The decompaction coefficient, $\alpha_r = 1 \cdot 10^{-9}$ $Pa^{-1}$ gives an effective compressibility that is 2 times the water compressibility. The porosity rebound from this decompaction coefficient is $\Delta\phi = \phi \alpha_r \rho_b g h = 0.26$ % when $h = 1000$ m of rock with porosity $\phi = 0.1$ is eroded under hydrostatic conditions using that $\rho_b = 2600$ $kg\,m^{-3}$ and zero uplift. Deglaciation of $400$ m ice under hydrostatic conditions gives a porosity rebound that is factor $0.16$ less, with other words $\Delta\phi = 0.04$ %. A larger decompaction coefficient gives a larger porosity rebound, but a larger porosity rebound may be difficult to reconcile with the sealing nature of the fractured overburden. The use of equation (34) to compute the present day underpressure indicates that the system must have low permeabilities for both the aquifer and the seal, and that the decompaction coefficient has to be larger than the water compressibility.

## 4.3 Compartment pressure through time

In order to see which period is the most important with respect to underpressure generation, we study the transient behaviour of the compartment model with the three stages of table 1, and with different scenarios of the aquifer permeability ($k_a$), seal permeability ($k_s$) and decompaction coefficient ($\alpha_r$). The solution (33) is used for time-stepping the pressure through the three time intervals: “œslow” erosion and unloading of 3.5 Ma, “rapid” deglaciation over 1 ka and then thermal cooling until today over 10 ka. The three intervals are summarized in table 1.

The study looks in turn at the two different seal permeabilities $1 \cdot 10^{-19}$ $m^2$ and $1 \cdot 10^{-21}$ $m^2$, where the lowest permeability is for a nearly impermeable seal [Neuzil, 1994]. For each seal permeability we compare the two decompaction coefficients $\alpha_r = 1 \cdot 10^{-9}$ $Pa^{-1}$ and $\alpha_r = 1 \cdot 10^{-8}$ $Pa^{-1}$ in combination with aquifer permeabilities over 5 orders of magnitude, from $1 \cdot 10^{-20}$ $m^2$

to $1 \cdot 10^{-15}$.

It is difficult to compare the transient behaviour of the three stages, because the time intervals are of different lengths (see table 1). Therefore, each of the three intervals is scaled to the unit interval, as shown in figures 6a-6d. The pressure during the first time interval is plotted in the left gray band from unit time 0 to 1. The pressure of the second and third time intervals are plotted in the center- and right bands, from unit time 1 to 2 and from unit time 2 to 3, respectively.

Before interpreting the transient results, it is worth recalling that a horizontal pressure curve is a stationary value. It is the case when the time interval is much longer than the characteristic time ($t_0$). A stationary pressure is more common during the first interval, because it is much longer than the two other time intervals. The value of the stationary pressure may be dominated by topographic driven flow, when the aquifer permeability is "large" compared to the seal permeability, as expressed by the condition $N_a >> N_s$. Next we have from approximation (7) that a linear decrease in the pressure means that the interval is short compared with the characteristic time. This takes place for the second and the third intervals, when we have that $\Delta t_2 = t_0$ or $\Delta t_3 = t_0$.

Figures 6a-6b show that the first interval of glacial erosion has stationary underpressure, which is seen as the flat pressure curves. Glacial erosion can create substantial underpressure that lasts until present time, when both the seal permeability and the aquifer permeability are towards their lower end values (see figures 6c-6d).

The second interval of deglaciation in figures 6a-6d is in a transient phase for all parameter choices (except for the largest aquifer permeability). This interval makes an important contribution to the present day underpressure. We notice that the pressure decrease during the interval does not seem to depend directly on the permeability. This follows from the estimate (8), which gives $\Delta p \approx 27$ bar when $\alpha_r = 2\alpha_f$, $\rho_f = 1000 \ \ kg\, m^{-3}$ and $h = 400$ m, as in figures 6a and 6c. In the case when $\alpha_r >> \alpha_f$ we get that $\Delta p \approx 40$ bar, as seen from figures 6b and 6d.

The third interval gives underpressure generation from thermal contraction. It contributes slightly to the underpressure for a low seal permeability as seen in figures 6c and 6d. The stationary pressure for thermal contraction is then lower than the underpressure generated during the interval of deglaciation.

The porosity rebound corresponding to the plots in figures 6a-c is shown in figures 7a-c, and it is computed using relation (30). Figures 7a-c show that porosity rebound in the initial transient regime and the stationary regime are weakly dependent on aquifer permeabilities. The total porosity rebound for the decompaction coefficient $\alpha_r = 1 \cdot 10^{-8} \ \ Pa^{-1}$ is in the range from $0.02$ to $0.05$, which may by too much for fracture rock to remain sealing. The decompaction $\alpha_r = 1 \cdot 10^{-9} \ \ Pa^{-1}$ gives an order of magnitude less porosity rebound, which seems more likely.

Appendix D shows how a stationary state of underpressure can be characterized by means of a gravity number, denoted $N_g$. A gravity number $N_g$ less than the porosity rebound $\Delta\phi$ tells that the stationary underpressure will be noticeable compared to the hydrostatic pressure difference over the aquifer, when the there is no topographic driven flow. The aquifer is 200 m thick, which gives a reference hydrostatic pressure of 20 bar. The gravity number for the first interval is $N_g = 0.1$ when $k_s = 1 \cdot 10^{-19}\ m^2$, which is too large for noticeable underpressure, when $\Delta\phi$ in the range from $0.003$ to $0.03$. A reduction of the seal permeability with two orders of magnitude gives the gravity number $N_g = 0.001$, which is sufficient to expect underpressure to develop. This interpretation is in agreement with underpressure shown in figures 6a and 6c.

## 5 A 2D basin model of Adventdalen

The compartment model assumes strata-bound fluid flow in the aquifers and vertical fluid flow in the subsurface of the valley. In order to better represent the geometry of the valley and the fluid flow in the subsurface we made a 2D basin model of the Adventdalen area. The 2D vertical cross section that follows the line shown in figure 1 was modelled. This line was selected because it contains well DH4 and it traverses the mountain to the neighbouring valley where the DeGeerdalen sandstone is exhumed.

It is difficult to find software that models glacial erosion coupled with fluid flow. We used the basin simulator BAS [Wangen, 2006], because it allows one to model erosion of the surface, and at the same time solves for pressure, when accounting for decompaction during unloading. This pressure equation is derived in Appendix A from conservation of solid and fluid, and it is solved with the potential along the dynamic topography as a Dirichlet boundary condition. The vertical boundaries and the base of the model were closed for fluid flow. The potential along the surface topography has a value produced by the height of the surface reduced with 100 m. This reduction in the potential represents a water table that is roughly 100 m below the surface due to permaforst.

A full basin model was build that deposited all layers since the end of Paleozoic. The present day geometry of the layers are shown in figure 8b. The layers were initially flat until the basin was uplifted, tilted and eroded flat between 36 Ma and 10 Ma. The Advendalen valley was eroded during the interval from 3.5 Ma until 100 ka. The basin simulator does not have any special features to handle glacial erosion by removing mass from the sediment surface underneath the ice. Therefore, the erosion and the growth of the last glacier were treated sequentially. The last glacial episode was modelled with the present day shape of the valley, by treating the growth of the last glacier as deposition of a sedimentary layer with the properties of ice. The ice builds up a constant rate until deglaciation starts at 11 ka, and deglaciation then last until 10 ka. The profile was at rest from 10 ka until present.

The main parameters in the modelling are a constant sandstone aquifer permeability $k_a = 1 \cdot 10^{-18} \ m^2$, a constant siltstone seal permeability $k_s = 1 \cdot 10^{-20} \ m^2$ and the decompaction coefficient $\alpha_r = 2 \cdot 10^{-9} \ Pa^{-1}$. The distribution of underpressure (as potential) at present time is shown in figure 8a. Underpressure is located underneath the base of the valley, where most of the unloading has taken place. Figure 8a shows the positive potential for topographic driven flow in the mountains and figure 8b also shows the layered lithologies and the present day Darcy flow field. The fluid flow is clearly strata bound in the aquifers and vertical in the low permeable siltstone underneath the base of the valley. The direction of the flow is clearly towards the point of lowest underpressure (or potential) as seen from figure 8b.

The last glaciation is modelled with growth of the ice from 100 ka to 11 ka, where the ice reaches a thickness of 400 m. This loading gives an overpressure of approximately $10$ bar. The period of deglaciation over the next 1 ka generates 40 bar underpressure, which is slightly reduced at present time. The deglaciation and the cooling until today are two stages where the pressure is in a transient state. Therefore, the present time underpressure is still in a transient state.

The pressure in the middle of the three sandstones in the DeGeerdalen (fm) at lateral position 519300 m is plotted in figure 9 as a function of time during the last 100 ka. The plot covers these three time intervals: (1) growth of the ice from 100 ka to 11 ka, (2) deglaciation from 11 ka to 10 ka and (3) cooling the subsurface from 10 ka until today. The slow erosion of the valley from 3.5 Ma to 100 ka is dominated by a slight overpressure from topographic driven flow, and this interval is not shown in figure 9. The pressure in the DeGeerdalen sandstone, plotted as a function of time in figure 9, has the basic behaviour as the three stage compartment model.

The basin modelling has a topographic driven flow from the mountain that is not captured by the compartment model by the height $h_m$ of the aquifer recharge area. The compartment model assumes that the aquifer is only charged where it is exhumed, and that the siltstone above the aquifer is completely sealing the aquifer from a topograpic driven flow from mountains above it. Figure 8b shows that there is a topographic driven flow from highest part of the mountain towards the base of the valley Adventdalen. The potential from the mountains above the aquifer is therefore more important than the potential where the aquifer is exhumed. A siltstone permeability equal to $k_s = 1 \cdot 10^{-20} \ m^2$ is not sufficient to seal the aquifer from topographic driven flow from the mountain. The compartment model reproduces the dynamics of the underpressured aquifer underneath the valley, but care has to be taken adjust the potential where the aquifer is exhumed.

## 6 Conclusions

Underpressure was discovered during drilling of a test well in the glacial valley Adventdalen at Svalbard. The cause for this underpressure is studied numerically with a basin model and

analytically with a compartment model. The 2D basin model simulates the geohistory of Adventdalen, and it accounts for underpressure generation underneath the valley and for the Darcy flow driven by the mountain topography surrounding the valley.

The pressure equation used in the basin model is derived from conservation of pore fluid and solid, in addition to constitutive relations for the fluid and the pore space. The compartment model is a pressure equation based on a simplified representation of the basin geometry. It allows one to analytically express under- and overpressure from a series of different unloading and loading intervals, when each interval is approximated with a constant erosion- and uplift rate. Our modelling takes into account the following three intervals: glacial erosion during Pliocene and Pleistocene, rapid deglaciation, and cooling of the subsurface during the Holocene until present time. The compartment model also gives expressions for the minimum and maximum pressure from cycles of glaciations.

Although the compartment model is a simple representation of the basin geometry, it has the same sink term for underpressure generation as the basin model. The different parts of the sink term that produce underpressure are identified as pore space rebound from unloading, fluid decompression from uplift and thermal expansion from cooling of the subsurface from erosion. These contributions are compared and our modelling suggests that pore space rebound dominates the two other contributions.

The compartment model gives the characteristic time for periods of underpressure generation that are represented by a constant erosion- and uplift-rate. The characteristic time tells whether the underpressured formation is in a transient state or a stationary state. Application of the compartment model to Adventdalen indicates that the valley had a stationary pressure close to the hydrostatic during the glacial erosion of the valley, when rapid fluctuations in the glacier thickness are ignored. The modelling suggests that the last deglaciation created a transient, which is the cause for the present day underpressure.

The compartment model also accounts for the topographic driven flow in terms of a recharge potential at a higher position in the aquifer. This position could be where the aquifer is exhumed in the neighbour valley, but the basin modelling results suggests that topographic driven flow from the neighbouring mountains is more important.

The stationary underpressure from the compartment model can be compared with the hydrostatic pressure difference over the aquifer, which leads to a dimensionless condition for underpressure. The condition is expressed in terms of the gravity number, and it is similar to a condition for overpressure build-up in sedimentary basins during deposition of sediments. The development of a noticeable underpressure requires that the gravity number is less than the porosity increment, which results from eroding a weight corresponding to the thickness of the seal.

We found that the current underpressure can be explained as a result of rebound of fracture porosity from the last deglaciation. Fracture porosity from deglaciation produces an order of magnitude stronger contribution to the sink term than thermal contraction. This conclusion is

also supported by the large number of fractures observed in the core samples of the DeGeerdalen formation [Ogata et al. , 2012]. The porosity rebound from deglaciation is estimated to be less than $0.1\%$ for a decompaction coefficient $\alpha_r = 1 \cdot 10^{-9} \ \ Pa^{-1}$. The maximum aquifer permeability is estimated to be $k_a = 1 \cdot 10^{-18} \ \ m^2$ and a maximum permeability for the seal is estimated to be $k_s = 1 \cdot 10^{-20} \ \ m^2$.

# 7 Appendix A: Pressure equation and fluid flow

The pressure equation is derived from mass conservation of fluid and solid in a porous medium, which gives that [Huyakorn Pinder, 1983, Wangen, 2010]

$$\frac{\phi}{\rho_f}\frac{D\rho_f}{dt} - \frac{\phi}{\rho_s}\frac{D\rho_s}{dt} + \frac{1}{\rho_f}\nabla\cdot(\rho_f \mathbf{v}_D) = -\frac{1}{(1-\phi)}\frac{D\phi}{dt}, \tag{13}$$

where $D/dt$ is the material derivative, $\phi$ is the porosity, $\rho_f$ is the fluid density, $\rho_s$ is the solid (matrix) density and $\mathbf{v}_D$ is the Darcy flux

$$\mathbf{v}_D = -\frac{k}{\mu}(\nabla p_f - \rho_f g \mathbf{n}_z). \tag{14}$$

To simplify the computation of a pressure that is different from the hydrostatic pressure we introduce the potential

$$\Phi = p_f - p_{h,0} \qquad and \qquad p_{h,0} = \int_0^z \rho_f g \, dz \tag{15}$$

where $p_{h,0}$ is the hydrostatic pressure for a water table at sea level. The usefulness of the potential $\Phi$ as the unknown is that it gives the underpressure directly, since the base of the valley Adventdalen is almost at sea level. In addition, the Darcy flux becomes potential flow, $\mathbf{v}_D = -(k/\mu)\nabla\Phi$, which is also a simplification. Writing the Darcy flux as potential flow assumes that the fluid density does not have any lateral variations, which could give rise to convective currents.

Conservation of the mass of fluid, as expressed by equation (13), needs expressions for $D\rho_f/dt$, $D\rho_s/dt$ and $D\phi/dt$ in order to become a complete pressure equation for a basin during uplift and erosion. The time-rate of change of fluid density is written

$$\frac{1}{\rho_f}\frac{D\rho_f}{dt} = \alpha_f\left(\frac{D\Phi}{dt} + \frac{Dp_{h,0}}{dt}\right) - \beta\frac{DT}{dt} \tag{16}$$

where $\alpha_{\mathrm{f}}$ is the fluid compressibility, $\beta$ is the fluid thermal expansion coefficient.

The thermal expansion coefficient for water is $\beta \approx 2 \cdot 10^{-4} \quad K^{-1}$ [Liley Gambill, 1973], and for common rocks it is $: 2 \cdot 10^{-5} \quad K^{-1}$ [Gilliam Morgan, 1988, Robertsen, 1988]. The thermal expansion of the rock matrix is an order of magnitude less than for water in the temperature interval from 20 $^{\circ}$C to 80 $^{\circ}$C and it is left out. The compressibility of water is often an order of magnitude larger than the compressibility of common minerals like quartz and calcite. Therefore, we assume that the density changes of the solid is less important than density changes of the fluid, and the term $D\rho_s/dt$ is ignored.

The rate of change of the porosity during unloading is treated in Appendix B. When expression (16) for the rate of change of density and equation (22) for the rate of change of porosity are inserted into the expression (13) for mass conservation, it gives the pressure equation

$$\phi\alpha_{\mathrm{eff}} \frac{\partial \Phi}{\partial t} - \nabla\left(\frac{k}{\mu}\nabla\Phi\right) = \phi\alpha_{\mathrm{eff}}\rho_f g\omega_u - \phi\beta\frac{\partial T}{\partial t} - \frac{\phi\alpha_r\rho_b g\omega}{1-\phi} \tag{17}$$

where the effective compressibility is

$$\alpha_{\mathrm{eff}} = \alpha_{\mathrm{f}} + \frac{\alpha_r}{1-\phi} \tag{18}$$

The material derivative of the potential is replaced by partial derivatives in the pressure equation (17), because small porosity changes imply negligible relative movements of the sediments in a vertical column [Wangen, 2010]. The pressure equation (17) is derived for underpressure generation during uplift and erosion. Underpressure is generated when the right-hand-side of equation (17) is a sink term (when it is less than zero). A similar pressure equation applies for pressure build-up during sediment deposition and compaction, but with the right-hand-side as a source term [Wangen, 2010].

# 8 Appendix B: Porosity rebound

The porosity rebound during unloading is taken to depend linearly on the reduction of effective vertical stress, as assumed by [Luo Vasseur, 1995]. The porosity increases with a small value

$$\Delta\phi = \phi_{\min}\alpha_r(\sigma'_{\max} - \sigma' \quad) \tag{19}$$

as the vertical effective stress $\sigma'$ decreases from its maximum value $\sigma'_{\max}$, where $\alpha_r$ is the mechanical decompaction coefficient. The mechanical decompaction coefficient is defined as

$$\alpha_r = \frac{1}{\phi_{\min}} \frac{\Delta\phi}{\Delta\sigma'_r} \tag{20}$$

for effective stress $\sigma'_r = \sigma'_{\max} - \sigma'$, when $\sigma'$ is decreasing from its maximum value $\sigma'_{\max}$. The rebound (19) can be viewed as an approximation to first order in the reduction of the vertical effective stress $\sigma'_{\max} - \sigma'$, which applies for small rebounds in the porosity. The vertical effective stress is the difference between lithostatic pressure $p_b$ and the fluid pressure $p_f$

$$\sigma' = p_b - p_f = p_b - p_{h,0} - \Phi \tag{21}$$

The time-derivative of the porosity becomes

$$\frac{D\phi}{dt} = \frac{d\phi}{d\sigma'} \frac{D\sigma'}{dt} = -\phi\alpha_r \left(\frac{Dp_b}{dt} - \frac{Dp_{h,0}}{dt} - \frac{D\Phi}{dt}\right) \tag{22}$$

The rate of change of the reference hydrostatic pressure can be expressed as

$$\frac{Dp_{h,0}}{dt} = -\rho_f g \omega_u \tag{23}$$

where $\omega_u$ is the uplift rate. The rate of change of the the overburden (the lithostatic pressure) can be written in the similar way as

$$\frac{Dp_b}{dt} = -\rho_f g \omega \tag{24}$$

where $\omega$ is the erosion rate. The uplift rate $\omega_u$ measures the velocity of the rock relative to the sea level, and the erosion rate $\omega$ measures how fast the rock surface retreats along a vertical relative to the rock. When the uplift rate and the erosion rates are equal the rock surface remains at the same height relative to sea level.

It is useful to consider the situations where uplift and erosion take place at near hydrostatic conditions. The rate of the porosity change can then be written

$$\frac{D\phi}{dt} = \phi\alpha_r g(\rho_b \omega - \rho_f \omega_u) \tag{25}$$

In the case that the uplift rate is equal to the erosion rate, we have that

$$\frac{D\phi}{dt} = \phi\alpha_r g(\rho_b - \rho_f)\omega \tag{26}$$

A similar expression for the rate change of porosity appears when erosion takes place without

any uplift ( $\omega_u = 0$ )

$$\frac{D\phi}{dt} = \phi\alpha_r g \rho_b \omega \tag{27}$$

Another observation is that the expressions (25) to (27) also hold for a stationary pressure state (where $\partial\Phi/\partial t = 0$). In either case, we have that the increase in porosity with time is proportional to the erosion rate.

Equation (19) is an expression for the porosity rebound since maximal burial. Maximum burial may have been around 36 Ma, when the Adventdalen area was uplifted and erosion started. The early uplift of Adventdalen which started after maximum burial was most likely a slow process. Assuming that the erosion kept pace with the uplift implies that the uplift rate and the erosion rate were about the same. The glacial loading and unloading produces an isostatic response, which considerably less than the thickness of the ice that filled the valley. The rate of unloading from deglaciation is considered more important the uplift from isostatic compensation that follows.

We are mainly interested in the rebound that are linked to glacial erosion and deglaciation, which took place during the last 3.5 Ma. The rebound at the beginning of glacial erosion can be written

$$\Delta\phi_1 = \phi\alpha_r \cdot (\sigma'_{\max} - p_{b,1} + p_{h,0} + \Phi_1) \tag{28}$$

where $p_{b,1}$ and $\Phi_1$ are the lithostatic pressure and potential at this time, respectively. The present day rebound is written in the same way

$$\Delta\phi_2 = \phi\alpha_r \cdot (\sigma'_{\max} - p_{b,2} + p_{h,0} + \Phi_2) \tag{29}$$

where $p_{b,2}$ and $\Phi_2$ are the present day lithostatic pressure and potential, respectively. We are interested in the rebound since the beginning of the glacial erosion, which becomes

$$\Delta\phi = \Delta\phi_2 - \Delta\phi_1 = \phi\alpha_r \cdot (-\Delta p_b + \Delta\Phi) \tag{30}$$

where the $\Delta p_b = p_{b,2} - p_{b,1}$ is the reduction in the lithostatic pressure, and $\Delta\Phi = \Phi_2 - \Phi_1$ is the change in the potential, and where both differences are with respect to the beginning of glacial erosion. The reference level for hydrostatic pressure is for simplicity assumed constant. Unloading gives reduction in the lithostatic pressure $\Delta p_b < 0$, which acts to increase the porosity rebound, while underpressure generation $\Delta\Phi < 0$ acts against porosity rebound. With respect increasing underpressure (decreasing potential) we assume that we are far away from reaching maximum effective vertical stress.

# 9 Appendix C: The pressure equation for the compartment model

Conservation of fluid mass for the underpressure compartment shown in figure 3 can be expressed as

$$\frac{d}{dt}(\phi l_2 h_2 \rho_f) = -\rho_f l_2 \frac{k_s}{\mu}\frac{p}{h_1} + \rho_f h_2 \frac{k_a}{\mu}\frac{(p_1 - p)}{l_1} \tag{31}$$

where the left-hand-side represents the increase in fluid mass in the compartment, while the right-hand-side represents the net mass flow of fluid into the compartment. This can be seen by multiplying the equation (31) by a small time step. The net flow into the compartment is the sum of the flow through the seal and the topographic driven flow from the aquifer. The compartment underpressure is denoted $p$, and the fluid potential where the aquifer is exhumed is denoted $p_1$. A contribution from the left hand side is neglected, because it is assumed to be less important than flow in the upward dipping aquifer at the right, because it is connected to the surface. A geometry of the model is shown in figure 3. The thickness of the sealing layer is $h_1$ and it has the permeability $k_s$. The aquifer, which holds the compartment, has the thickness $h_2$ and the aquifer permeability $k_a$. The aquifer extends a distance $l_1$ to the left, where it is exhumed in the neighbouring valley, and the length of the compartment is $l_2$. The height $h_2$ depends on the porosity, and it is $h_2 = \zeta_2/(1-\phi)$, where $\zeta_2$ is the net (porosity free) thickness of the aquifer. The time-derivation can the be carried out, and $d\rho_f/dt$ and $d\phi/dt$ can be replaced by expressions (16) and (22), respectively, and the result becomes equation (1).

Equation (1) for the underpressure has the general solution

$$p(t) = p_0 \cdot \exp(-t/t_0) + \int_0^t \exp((t'-t)/t_0)\, p_s(t')dt' \tag{32}$$

where $p_0$ is the (initial) underpressure at time $t = 0$. The pressure solution (32) applies for any time-dependent erosion rate $\omega(t)$ and uplift rate $\omega_u(t)$. In the case $p_s(t)$ is constant the solution simplifies to

$$p(t) = p_0 \cdot \exp(-t/t_0) + p_s \cdot (1 - \exp(-t/t_0)) \tag{33}$$

The solution (33) shows how the characteristic time controls the decay of the initial pressure, and the transient towards a new stationary state with underpressure $p_s$. The general solution (32) is useful when $p_s(t)$ is known, as for instance when $p_s(t)$ is piecewise constant, where each time interval has its own $p_s$-value.

The present day underpressure in the compartment, for three intervals of unloading, can be computed by adding together the contributions from all three intervals. By treating the

intervals sequentially in time with solution (33), where the pressure at the end of one interval becomes the initial pressure in the following interval, gives the present day underpressure. Alternatively, the present day pressure can be obtained from solution (32), using piecewise constant stationary pressures for each interval. In any case, the present day underpressure becomes

$$p_3 = p_{\omega,1} \cdot (1 - \exp(-\Delta t_1/t_0)) \cdot \exp(-(\Delta t_2 + \Delta t_3)/t_0)$$

$$+ p_{\omega,2} \cdot (1 - \exp(-\Delta t_2/t_0)) \cdot \exp(-\Delta t_3/t_0)$$

$$+ p_{\omega,3} \cdot (1 - \exp(-\Delta t_3/t_0))$$

$$+ p_m \cdot (1 - \exp(-(\Delta t_1 + \Delta t_2 + \Delta t_3)/t_0)) \quad (34)$$

The pressure $p_{\omega,1}$, $p_{\omega,2}$ and $p_{\omega,3}$ are the three stationary underpressures for each of the three time intervals, and $p_m$ is the stationary potential from topographic driven fluid flow.

The pressure solution (33) can also handle the pressure build-up and pressure decrease during cycles of loading and unloading, respectively. If the same cycle repeats itself again and again the pressure will oscillate between an upper and a lower pressure limits. These limits can be found as initial conditions of two pressure solution (33), where one initial condition is for the pressure build-up towards a stationary pressure $p_{s,a}$, and the other is the initial condition $p_2$ for pressure decline towards a stationary solution $p_{s,b}$. We then have that

$$p_1 = p_{s,a} + (p_2 - p_{s,a}) \exp(-\tau_a) \quad (35)$$

$$p_2 = p_{s,b} + (p_1 - p_{s,b}) \exp(-\tau_b) \quad (36)$$

where $p_1$ is the initial pressure for the second interval, while final pressure of second interval $p_2$ is the initial value for the first interval. The time spans of the two intervals of a cycle are $\tau_a$ and $\tau_b$, respectively, and a full cycle has the period $\tau_a + \tau_b$. The stationary pressure for the first interval is $p_{s,a}$ and the second it is $p_{s,b}$. Solving for the end-values $p_1$ and $p_2$ gives

$$p_1 = \frac{p_{s,a} + (p_{s,b} - p_{s,a}) \exp(-\tau_a) - p_{s,b} \exp(-\tau_a - \tau_2)}{1 - \exp(-\tau_a - \tau_b)} \quad (37)$$

$$p_2 = \frac{p_{s,b} + (p_{s,a} - p_{s,b}) \exp(-\tau_b) - p_{s,a} \exp(-\tau_a - \tau_b)}{1 - \exp(-\tau_a - \tau_b)} \quad (38)$$

The case where the intervals last much longer than the characteristic time ($\tau_a >> 1$ and $\tau_b >> 1$) implies that the pressure oscillates between the two stationary values, because

$p_1 \approx p_{s,a}$ and $p_2 \approx p_{s,b}$.

## 10 Appendix D: Condition for underpressure

It is possible to formulate a condition for underpressure generation, which is similar to a condition for overpressure build-up in sedimentary basins during burial and deposition of sediments. Overpressure build-up from porosity reduction during burial is the opposite process of underpressure generation during uplift, erosion and decompaction. The condition for underpressure assumes that the overburden is eroded at a constant rate, with a stationary compartment underpressure caused by decompaction. It is also assumed that the underpressure is controlled by the seal and that topographic driven fluid flow is negligible ($N_a = 0$). The stationary underpressure in the compartment, equation (5), can then be compared with the hydrostatic pressure difference across the compartment, $\rho_f g h_2$, which is taken as the reference pressure. The condition for underpressure is stated as $|\, p_f \,| > \rho_f g h_2$, which is

$$\frac{\phi \mu \alpha_r \rho_b g \omega}{(1-\phi) N_s} > \rho_f g h_2 \tag{39}$$

for zero uplift ($\omega_u = 0$), isothermal conditions ($\partial T/\partial t = 0$) and no topographic driven fluid flow ($N_a = 0$). The condition (39) can be expressed on a dimensionless form in terms of the gravity number $N_g$ as

$$N_g = \frac{\rho_f g k_s}{\mu \omega} < \frac{\phi \alpha_r g \rho_b h_1}{1-\phi} = \frac{\Delta\phi}{1-\phi} \approx \Delta\phi \tag{40}$$

for porosities in the range $0$ to $0.2$. The porosity rebound $\Delta\phi = \phi \alpha_r g \rho_b h_1$ is the expansion that follows from the erosion of a thickness equal to the seal under hydrostatic pressure. The condition for underpressure (40) is stated as $N_g < \Delta\phi$ by use of the gravity number $N_g = \rho_f g k_s/(\mu\omega)$. This condition is similar to the condition for overpressure build-up during deposition of sediments, which is $N_g$ **=** $1$, [Audet Fowler, 1992, Audet, 1995, Wangen, 1992, Wangen, 1997, Wangen, 2001]. The latter condition is derived for 1D models in the vertical direction with just one (average) lithology. In these 1D models, the overpressure is measured at the base of the sedimentary column, where it is at maximum. Generation and dissipation of overpressure may take place over time spans of 100 million years or more, and the porosity is reduced from its initial surface porosity ($: 0.5$) to the low porosity of fully compacted rock ($: 0.05$) at the base of the basin. The similarity between the two conditions is that both require the gravity number to be less than a threshold. The difference is that the expansion of the porosity during periods of erosion and unloading is small compared to the porosity reduction

from the basin surface to the base. The threshold $\Delta\phi/(1-\phi)$ is of order $1$ for the case of overpressure build-up. Another difference is that overpressure is measured against the difference between the lithostatic pressure and the hydrostatic pressure, while absolute value of the underpressure is measured against hydrostatic pressure.

## 11 Acknowledgements

The authors are grateful to Hans Borge (University of Stavanger), two anonymous referees for their constructive reviews of the manuscript, and to Alvar Braathen (University of Oslo) for data and interpretations.

This work has been partially funded by the SUCCESS center for CO2 storage under grant 193825/S60 from Research Council of Norway (RCN). SUCCESS is a consortium with partners from industry and science, hosted by Christian Michelsen Research as.

## References

[Audet, 1995] Audet, D.M. 1995. Mathematical-modeling of gravitational compaction and clay dehydration in thick sedimentary layers. *Geophysical Journal International*, **122**, 283-298.

[Audet Fowler, 1992] Audet, D.M., & Fowler, A.C. 1992. A mathematical model for compaction in sedimentary basins. *Geophysical Journal International*, **110**, 577-590.

[Bachu Underschultz, 1995] Bachu, S, & Underschultz, JR. 1995. Large-scale underpressuring in the Mississippian-Cretaceous succession, Southwestern Alberta Basin. *AAPG Bulletin*, **79**(7), 989-1004.

[Bekele et al. , 2003] Bekele, EB, Rostron, BJ, & Person, MA. 2003. Fluid pressure implications of erosional unloading, basin hydrodynamics and glaciation in the Alberta Basin, Western Canada. *Journal of Geochemical Exploration*, **78-9**(SI), 143-147. Geofluids IV Meeting, Utrecht, Netherlands, May 12-16, 2003.

[Belitz Bredehoeft, 1988] Belitz, K., & Bredehoeft, J. 1988. Hydrodynamics of Denver Basin: explanation of subnormal fluid pressures. *AAPG Bulletin*, **72**(11), 1334-1359.

[Bense Person, 2008] Bense, V.F., & Person, M.A. 2008. Transient hydrodynamics within intercratonic sedimentary basins during glacial cycles. *Journal of Geophysical Research*, **113**, F04005.

[Borge, 2002] Borge, H. 2002. Modelling generation and dissipation of overpressure in sedimentary basins: An example from Halten Terrace, offshore Norway. *Marine and Petroleum Geology*, **19**, 377-388.

[Braathen et al. , 2012] Braathen, A., Balum, K., Christiansen, H.H., Dahl, T., Eiken, O., Elvebakk, H., Hansen, F., Hanssen, T.H., Jochmann, M., Johansen, T.A., Johnsen, H., Larsen, L., Lie, T., Mertes, J., Mork, A., Mork, M.B., Nemec, W., Olaussen, S., Oye, V., Rod, K., Titlestad, G.O., Tveranger, J., & Vagle, K. 2012. The Longyearbyen CO2 Lab of Svalbard, Norway - Initial assessment of the geological conditions for CO2 sequestration. *Norwegian Journal of Geology*, **92**, 353 - 376.

[Bradley, 1975] Bradley, J.S. 1975. Abnormal formation pressure. *AAPG Bulletin*, **59**, 957-973.

[Chapman, 1976] Chapman, D. 1976. *Abnormal pore pressures: essential theory possible causes*

*and sliding*. Developments in Petroleum Science, 38. Elsevier. Chap. 3, pages 51-88.

[Corbet Bethke, 1992] Corbet, T.F., & Bethke, C.M. 1992. Disequilibrium fluid pressures and groundwater flow in western Canada sedimentary basin. *Journal of Geophysical Research*, **97**(B5), 7203-7217.

[Dickey Cox, 1977] Dickey, P.A., & Cox, W.C. 1977. Oil and gas in reservoirs with subnormal pressures. *AAPG Bulletin-American Association of Petroleum Geologists*, **61**(12), 2134-2142.

[Eiriksson, 2008] Eiriksson, Jon. 2008. Glaciation events in the Pliocene - Pleistocene volcanic succession of Iceland. *JOKULL*, **58**, 315-329.

[Elvebakk, 2010] Elvebakk, H. 2010. *Results of borehole logging in well LYB CO2, Dh4 of 2009, Longyearbyen, Svalbard*. Tech. rept. 2010.018. Geological Survey of Norway.

[Geirsdottir, 2011] Geirsdóttir, Á. 2011. Chapter 16 - Pliocene and Pleistocene Glaciations of Iceland: A Brief Overview of the Glacial History. *Pages 199 - 210 of:* Jürgen Ehlers, Philip L. Gibbard, & Hughes, Philip D. (eds), *Quaternary Glaciations - Extent and Chronology A Closer Look*. Developments in Quaternary Sciences, vol. 15. Elsevier.

[Gilliam Morgan, 1988] Gilliam, T. M., & Morgan, I. L. 1988. *Shale: measurement of thermal properties*. Tech. rept. ORNL/TM-10499. Oak Ridge National Laboratory.

[Hall, 1994] Hall, P.L. 1994. Physical and chemical aspects of the development of overpressuring in sedimentary environments. *Clay Minerals*, **29**(4), 425-437.

[Hambrey Glasser, 2012] Hambrey, Michael J., & Glasser, Neil F. 2012. Discriminating glacier thermal and dynamic regimes in the sedimentary record. *Sedimentary Geology*, **251 - 252**(0), 1 - 33.

[Huyakorn Pinder, 1983] Huyakorn, P.S., & Pinder, G.F. 1983. *Computational methods in subsurface flow*. Monograph Series. Academic Press.

[Iverson Person, 2012] Iverson, N., & Person, M. 2012. Glacier-bed geomorphic processes and hydrologic conditions relevant to nuclear waste disposal. *Geofluids*, **12**, 38-57.

[Lazear, 2009] Lazear, Gregory D. 2009. Fractures, convection and underpressure: hydrogeology on the southern margin of the Piceance basin, west-central Colorado, USA. *Hydrogeology Journal*, **17**(3), 641-664.

[Lemieux et al. , 2008a] Lemieux, J-M., Sudicky Peltier, W.R., & Tarasov, L. 2008a. Dynamics of groundwater recharge and seepage over the Canadian landscape during the Wisconsinian glaciation. *Journal of Geophysical Research*, **113**, F01011.

[Lemieux et al. , 2008b] Lemieux, J-M., Sudicky Peltier, W.R., & Tarasov, L. 2008b. Simulating the impact of glaciations on continental groundwater flow systems: I. Relevant processes and

model formulation. *Journal of Geophysical Research*, **113**, F03017.

[Lemieux et al. , 2008c] Lemieux, J-M., Sudicky Peltier, W.R., & Tarasov, L. 2008c. Simulating the impact of glaciations on continental groundwater flow systems: II. Model application to the Wisconsinian glaciation over the Canadian landscape. *Journal of Geophysical Research*, **113**, F03018.

[Liley Gambill, 1973] Liley, P.E., & Gambill, W.R. 1973. *Chemical Engineering Handbook*. McGraw-Hill. Chap. 3, pages 101-108.

[Lou Vasseur, 1992] Lou, X.R., & Vasseur, G. 1992. Contributions of compaction and aquathermal pressuring to geopressure and the influence of environmental-conditions. *AAPG Bulletin*, **76**(10), 1550-1559.

[Luo Vasseur, 1995] Luo, XR, & Vasseur, G. 1995. Modeling of pore pressure evolution associated with sedimentation and uplift in sedimentary basins. *Basin Research*, **7**(1), 35-52.

[Luthi Funk, 2013] Lüthi, M., & Funk, M. 2013. *Physics of Glaciers I: Chapter 6: Temperatures in glaciers and ice sheets*. Tech. rept. 651-4101-00 / HS 2013. Versuchsanstalt fï¿½r Wasserbau, Hydrologie und Glaziologie.

[Neuzil, 1994] Neuzil, CE. 1994. How permeable are clays and shales. *Water Resources Research*, **30**(2), 145-150.

[Neuzil Pollock, 1983] Neuzil, C.E., & Pollock, D.W. 1983. Erosional unloading and fluid pressures in hydraulically tight rocks. *Journal of Geology*, **91**(2), 179-193.

[Ogata et al. , 2012] Ogata, K., Senger, K., Braathen, A., Tveranger, J., & Olaussen, S. 2012. The importance of natural fractures in a tight reservoir for potential CO2 storage: a case study of the upper Triassic-middle Jurassic Kapp Toscana Group (Spitsbergen, Arctic Norway). *Geological Society, London, Special Publications published online*, **374**(September 10), 1 - 21.

[Orr Kreitler, 1985] Orr, ED, & Kreitler, CW. 1985. Interpretation of pressure-depth data from confined underpressured aquifers exemplified by the deep-basin brine aquifer, Palo Duro basin, Texas. *Water Resources Research*, **21**(4), 533-544.

[Parks Toth, 1995] Parks, KP, & Toth, J. 1995. Field evidence for erosion-induced underpressuring in upper cretaceous and tertiary strata, West Central Alberta, Canada. *Bulletin of Canadian Petroleum Geology*, **43**(3), 281-292.

[Paus, 1989] Paus, A. 1989. Late Weichselian vegetation, climate and floral migration at Eigebakken, South Rogaland, Southwestern Norway. *Review of Palaeobotany and Palynology*, **61**(3-4), 177 - 203.

[Petit et al. , 1999] Petit, J. R., Jouzel, J., Raynaud, D., Barkov, N. I., , Barnola, J.-M., Basile, I., Bender, M., Chappellaz, J., Davis, M., Delaygue, G., Delmotte, M., Kotlyakov, V. M., Legrand, M.,

Lipenkov, V. Y., Lorius, C., Pépin, L., Ritz, C., Saltzman, E., & Stievenard, M. 1999. Climate and atmospheric history of the past 420,000 years from the Vostok ice core, Antarctica. *Nature*, **399**, 429-436.

[Robertsen, 1988] Robertsen, E.C. 1988. *Thermal properties of rocks*. Tech. rept. Open-File 88-441. United States Department of the Interior, Geological Survey.

[Russell, 1972] Russell, W.L. 1972. Pressure-depth relations in Appalachian region. *AAPG Bulletin*, **56**(3), 528-536.

[Sharp, 1988] Sharp, R.P. 1988. *Living ice: Understanding glaciers and glaciation*. American Elsevier, New York.

[Skirbekk et al. , 2010] Skirbekk, K., Klitgaard-Kristensen, D., Rasmussen, T.L., Koc, N., & Forwick, M. 2010. Holocene climate variations at the entrance to a warm Arctic fjord: evidence from Kongsfjorden trough, Svalbard. *Geological Society Special Publication*, **344**, 289 - 304.

[Starkel, 2003] Starkel, L. 2003. Younger Dryas-Preboreal transition documented in the fluvial environment of Polish rivers. *Global and Planetary Change*, **35**(1?2), 157 - 167.

[Swarbrick Osborne, 1997] Swarbrick, R.E., & Osborne, M.J. 1997. Mechanisms for generating overpressure in sedimentary basins: A reevaluation. *AAPG Bulletin*, **81**(6), 1023-1041.

[Toth, 1978] Toth, J. 1978. Gravity-induced cross-formational flow of formation fluids, Red Earth region, Alberta, Canada - Analysis, patterns, and evolution. *Water Resources Research*, **14**(5), 805-843.

[USGS, 2014] USGS. 2014. *The Land Processes Distributed Active Archive Center (LP DAAC), http://gdex.cr.usgs.gov/gdex/*.

[Vinard et al. , 2001] Vinard, Pascal, Bobet, Antonio, & Einstein, Herbert H. 2001. Generation and evolution of hydraulic underpressures at Wellenberg, Switzerland. *Journal of Geophysical Research: Solid Earth*, **106**(B12), 30593-30605.

[Wangen, 1992] Wangen, M. 1992. Pressure and temperature evolution in sedimentary basins. *Geophysics Journal International*, **110**, 601-613.

[Wangen, 1997] Wangen, M. 1997. Simple model of pressure build-up during burial. *Geophysical Journal International*, **130**, 757-764.

[Wangen, 2001] Wangen, M. 2001. A quantitative comparison of some mechanisms generating overpressure in sedimentary basins. *Tectonophysics*, **334**, 211-234.

[Wangen, 2006] Wangen, M. 2006. *User”™s guide to Bas, version 14.0*. Tech. rept. Institute for Energy Technology, Kjeller, Norway.

[Wangen, 2010] Wangen, M. 2010. *Physical Principles of Sedimentary Basin Analysis*. Cambridge University Press.

## Tables

| **Interval:** | **1** | **2** | **3** |
|---|---|---|---|
| Process: | Glacial erosion | Deglaciation | Rest |
| Time [ka]: | from 3500 to 11 | from 11 to 10 | from 10 to 0 |
| Unloading: | yes | yes | no |
| Cooling: | yes | no | yes |

Table 1: The three intervals in the three-stage model.

| Parameter | Value | Units |
|---|---|---|
| initial res. pres. (p0) | 0 | [Pa] |
| height aquifer recharge (hm) | 300 | [m] |
| thickness seal (h1) | 500 | [m] |
| thickness reservoir (h2) | 200 | [m] |
| length aquifer (l1) | 15000 | [m] |
| length compartment (l2) | 2000 | [m] |
| uplift rate (ωu) | 0 | [m/Ma] |
| burial rate (ω1) | 285.714 | [m/Ma] |
| burial rate (ω2) | 800000 | [m/Ma] |
| burial rate (ω3) | 11111.1 | [m/Ma] |
| porosity (φ) | 0.1 | [-] |
| viscosity (μ) | 0.001 | [Pa s] |
| density fluid ($\rho_f$) | 1000 | [kg/m3] |
| density bulk matrix ($\rho_b$) | 2600 | [kg/m3] |
| compress. fluid (α) | 5e-10 | [1/Pa] |
| thermal exp. fluid (β) | 0.0002 | [1/K] |
| thermal gradient. (dT/dz) | 0.045 | [C/m] |
| gravity (g) | 10 | [m/s2] |

Table 2: The decompaction coefficient, the aquifer permeability and the seal permeability are not well constrained parameters. The burial rate $\omega_2$ is corrected with respect to the weight of the ice and the rate $\omega_3$ is used to provide cooling of the compartment after the ice melted.

Figure 1: The topography of Adventdalen at Svalbard [USGS, 2014]. The white dot marks well DH4 and the line shows the vertical cross section that is simulated with the basin model.

Figure 2: The lithostratigraphy of well DH4. The fluid pressure is compared with hydrostatic pressure that is zero at the surface, even though the actual hydrostatic pressure is reduced by roughly 15 bar because of permafrost.

Figure 3: A sketch of the compartment model for underpressure generation. There are two fluxes that tries to balance the underpressure generation: vertical flow from the hydrostatic aquifer downwards through the seal and topographic driven flow in the aquifer. The length of the aquifer is l1 and the width of the underpressure compartment is l2.

Figure 4: Pressure transients during cycles of loading and unloading. The time intervals of loading and unloading are scaled to the unit interval. (a) Time for loading is longer than the characteristic time of the system and the stationary state is nearly reached. The time for unloading is shorter than the characteristic time. (b) Both the time for loading and unloading are shorter than the characteristic time.

Figure 5: The compartment pressure after the three time intervals in table 1 for different choices of the aquifer pressure $k_a$ and seal pressure $k_s$. The figures (a), (b) and (c) have decompaction coefficients $\alpha_r = 1 \cdot 10^{-10}\ \ Pa^{-1}$, $1 \cdot 10^{-9}\ \ Pa^{-1}$ and $1 \cdot 10^{-8}\ \ Pa^{-1}$, respectively.

Figure 6: The transients of the underpressure during three stages of unloading for different aquifer permeabilities, seal permeabilities and decompaction coefficients. The time span of the stages is of very different length. In order to plot the pressure evolution during the three stages in the same plot each stage has the time scaled to the unit interval. (The x-axis is therefore from 0 to 3.) The seal permeability and decompaction coefficient differ as follows: (a) $k_s = 1 \cdot 10^{-19}\ \ m^2$ and $\alpha_r = 1 \cdot 10^{-9}\ \ Pa^{-1}$. (b) $k_s = 1 \cdot 10^{-19}\ \ m^2$ and $\alpha_r = 1 \cdot 10^{-8}\ \ Pa^{-1}$. (c) $k_s = 1 \cdot 10^{-21}\ \ m^2$ and $\alpha_r = 1 \cdot 10^{-9}\ \ Pa^{-1}$. (d) $k_s = 1 \cdot 10^{-21}\ \ m^2$ and $\alpha_r = 1 \cdot 10^{-8}\ \ Pa^{-1}$. Additional parameters are collected in table 1.

Figure 7: The porosity evolution for the same cases of unloading through three stages as shown in figure 6. The time span of the stages is of very different length. In order to plot the pressure evolution during the three stages in the same plot each stage has the time scaled to the unity interval. (The x-axis is therefore from 0 to 3.) The seal permeability and decompaction coefficient differ as follows: (a) $k_s = 1 \cdot 10^{-19} \ \ m^2$ and $\alpha_r = 1 \cdot 10^{-9} \ \ Pa^{-1}$. (b) $k_s = 1 \cdot 10^{-19} \ \ m^2$ and $\alpha_r = 1 \cdot 10^{-8} \ \ Pa^{-1}$. (c) $k_s = 1 \cdot 10^{-21} \ \ m^2$ and $\alpha_r = 1 \cdot 10^{-9} \ \ Pa^{-1}$. (d) $k_s = 1 \cdot 10^{-21} \ \ m^2$ and $\alpha_r = 1 \cdot 10^{-8} \ \ Pa^{-1}$. Addition parameters are collected in table 1.

Figure 8: (a) The plot shows the present day potential, where the potential underneath the base of the valley is close to the difference between fluid pressure and hydrostatic pressure. The potential gets units meter by diving its value in Pa by $10^4$. (b) The plot shows the vertical crossection with lithologies and the fluid flow field at present time.

Figure 9: A comparison of the pressure evolution in DeGeerdalen fm when it is modelled with basin model and the compartment model. The three unit intervals are (1) growth of the ice since 100 ka, (2) deglaciation over 1 ka (3) cooling of the subsurface until today.

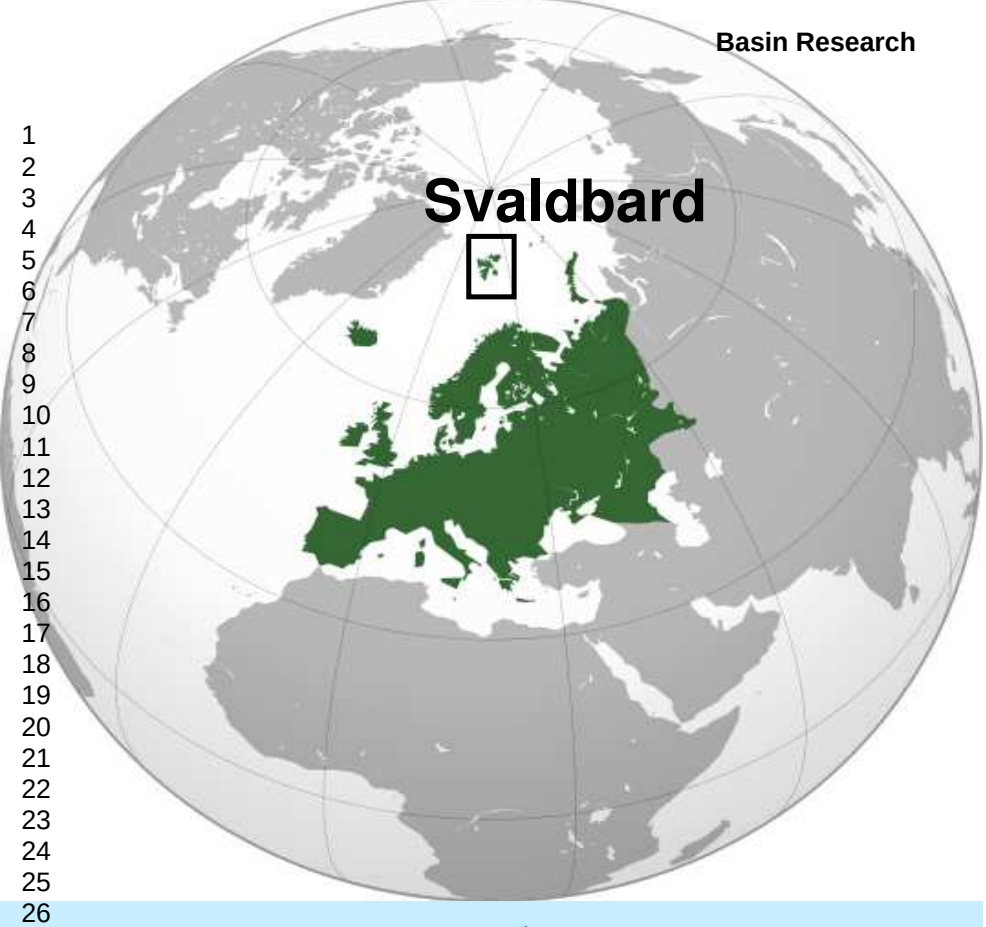



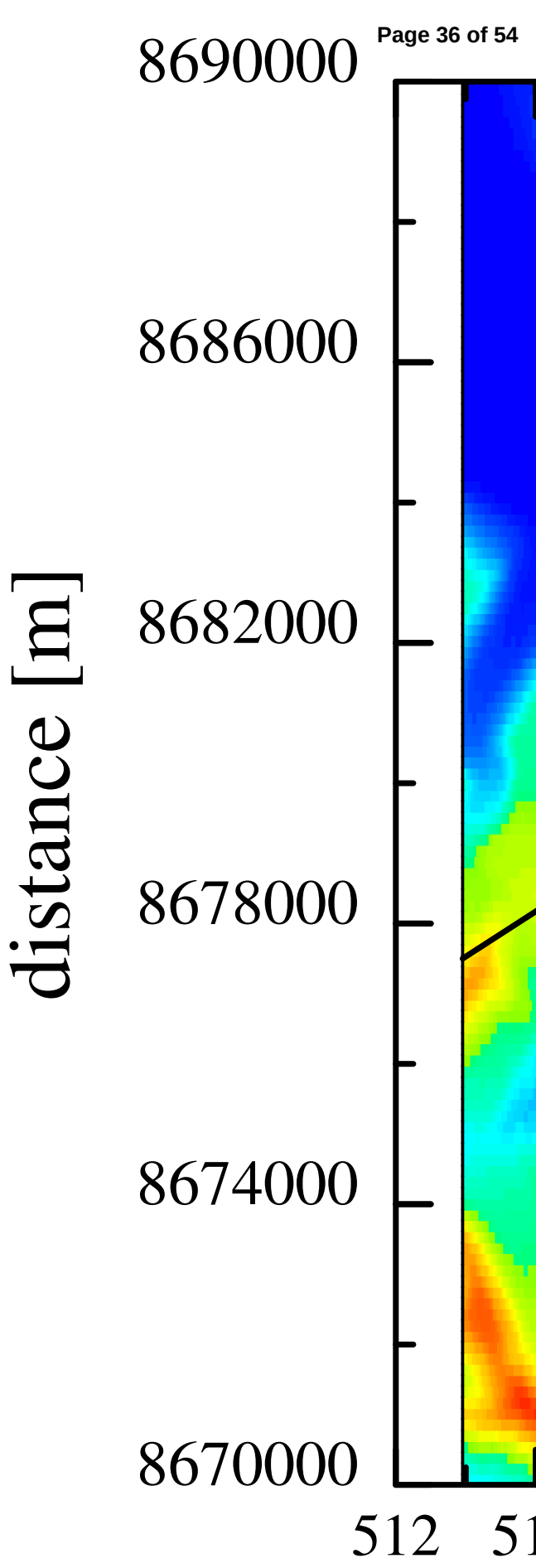

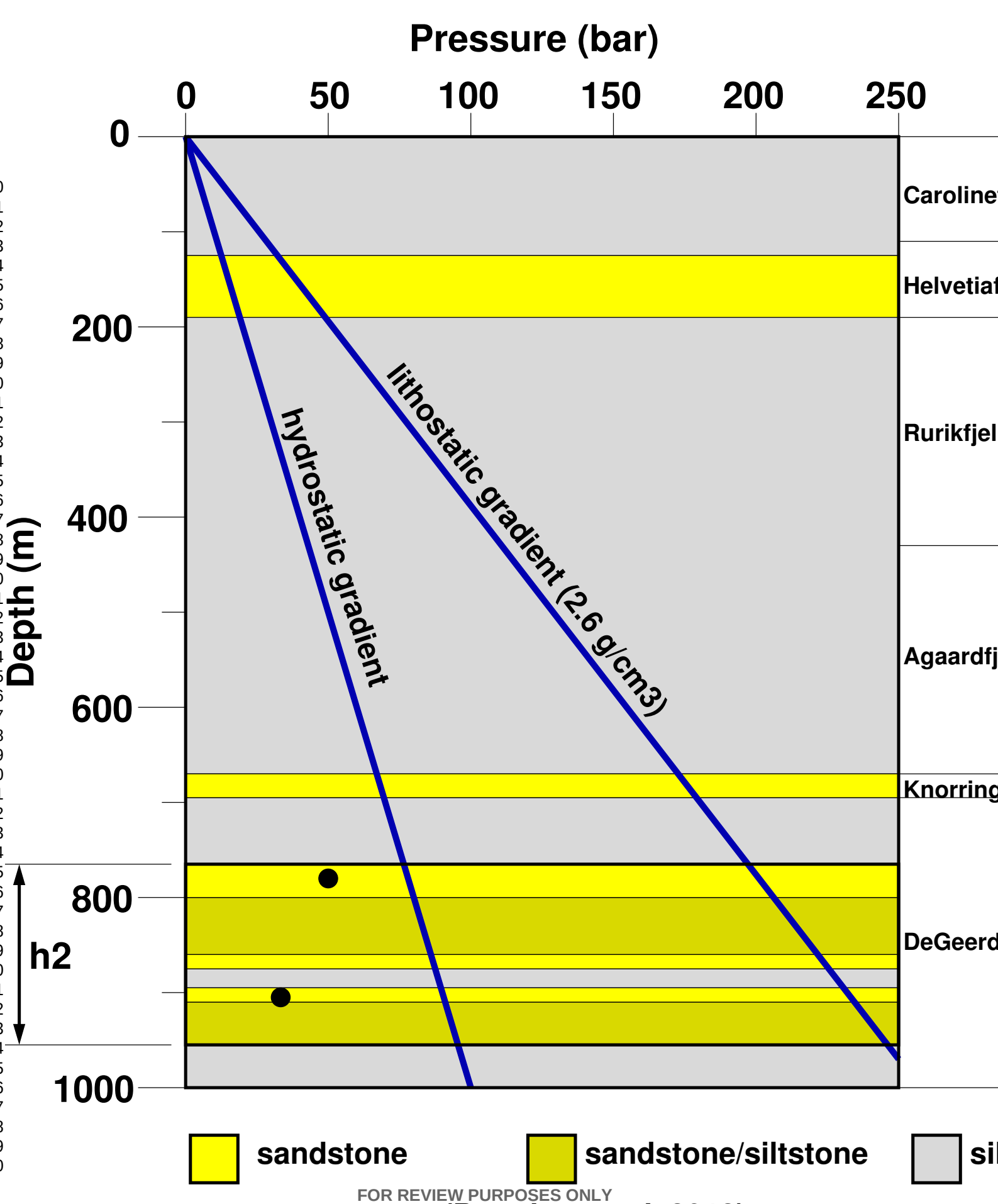

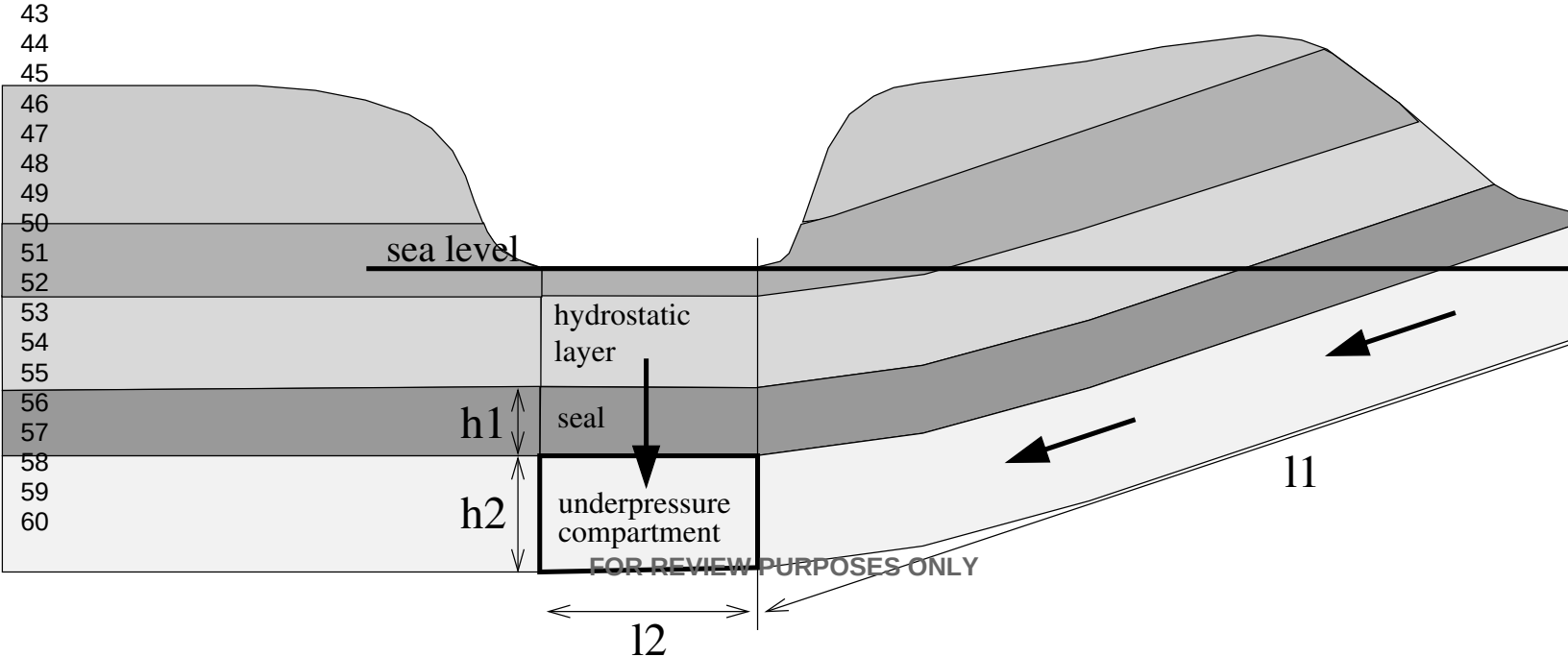

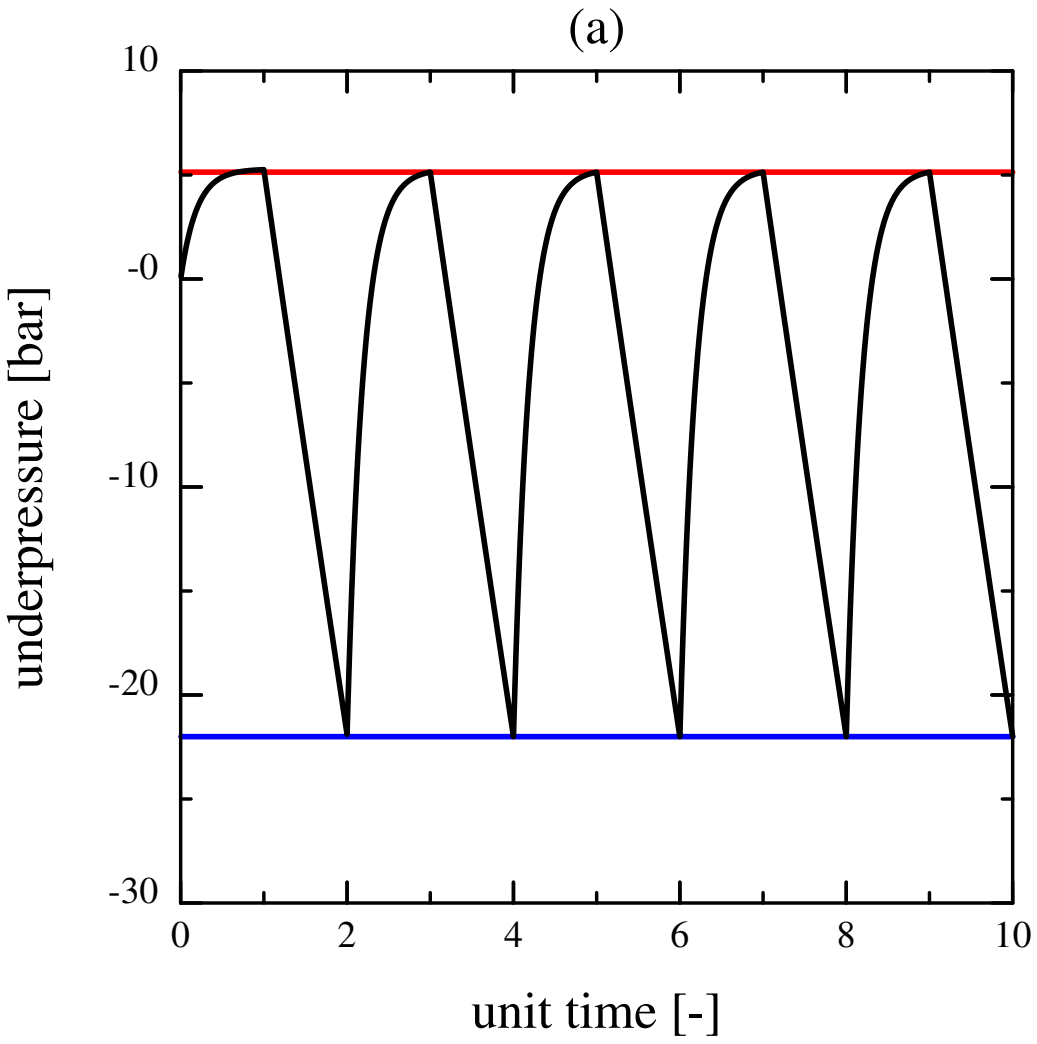
(a)
10
-0
-10
-20
-30
0
2
4
6
8
10
underpressure [bar]
unit time [-]

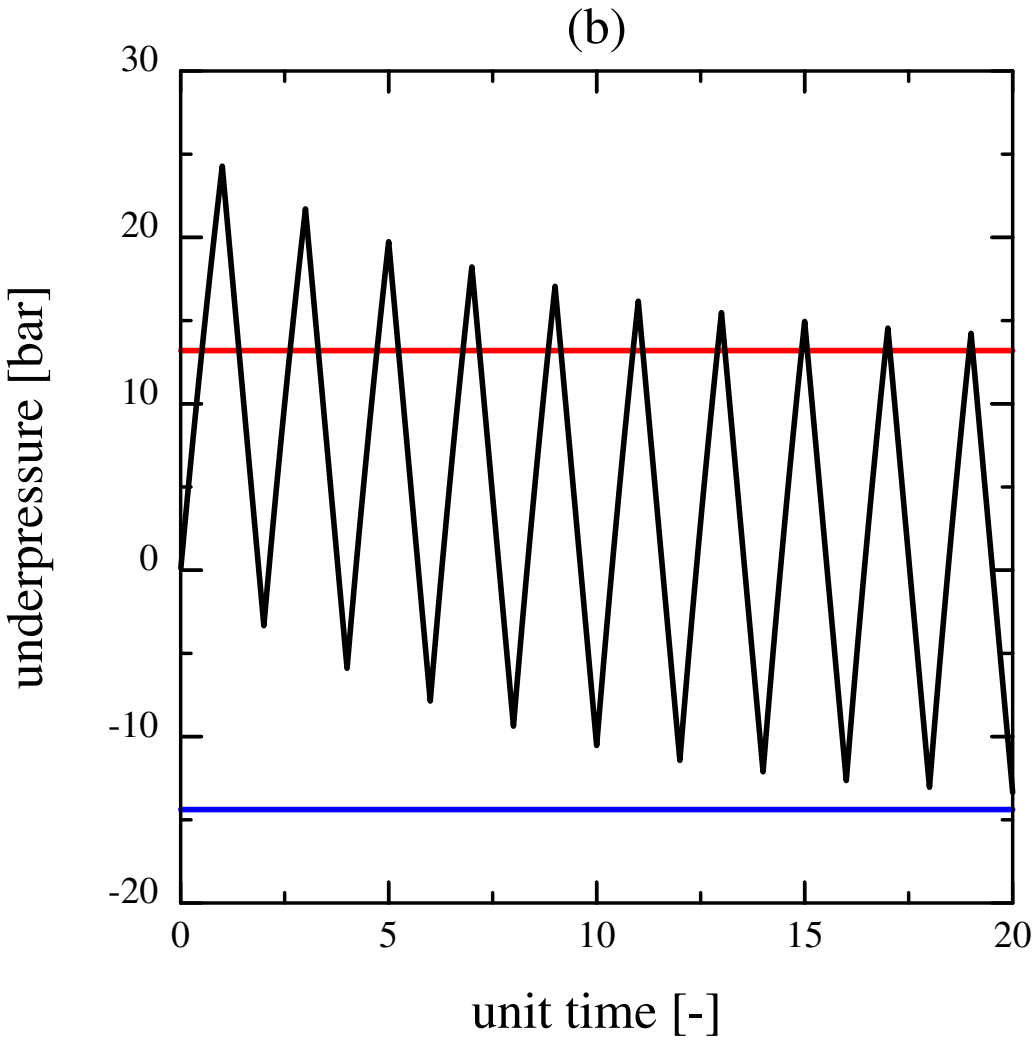
(b)
30
20
10
0
-10
-20
0
5
10
15
20
underpressure [bar]
unit time [-]

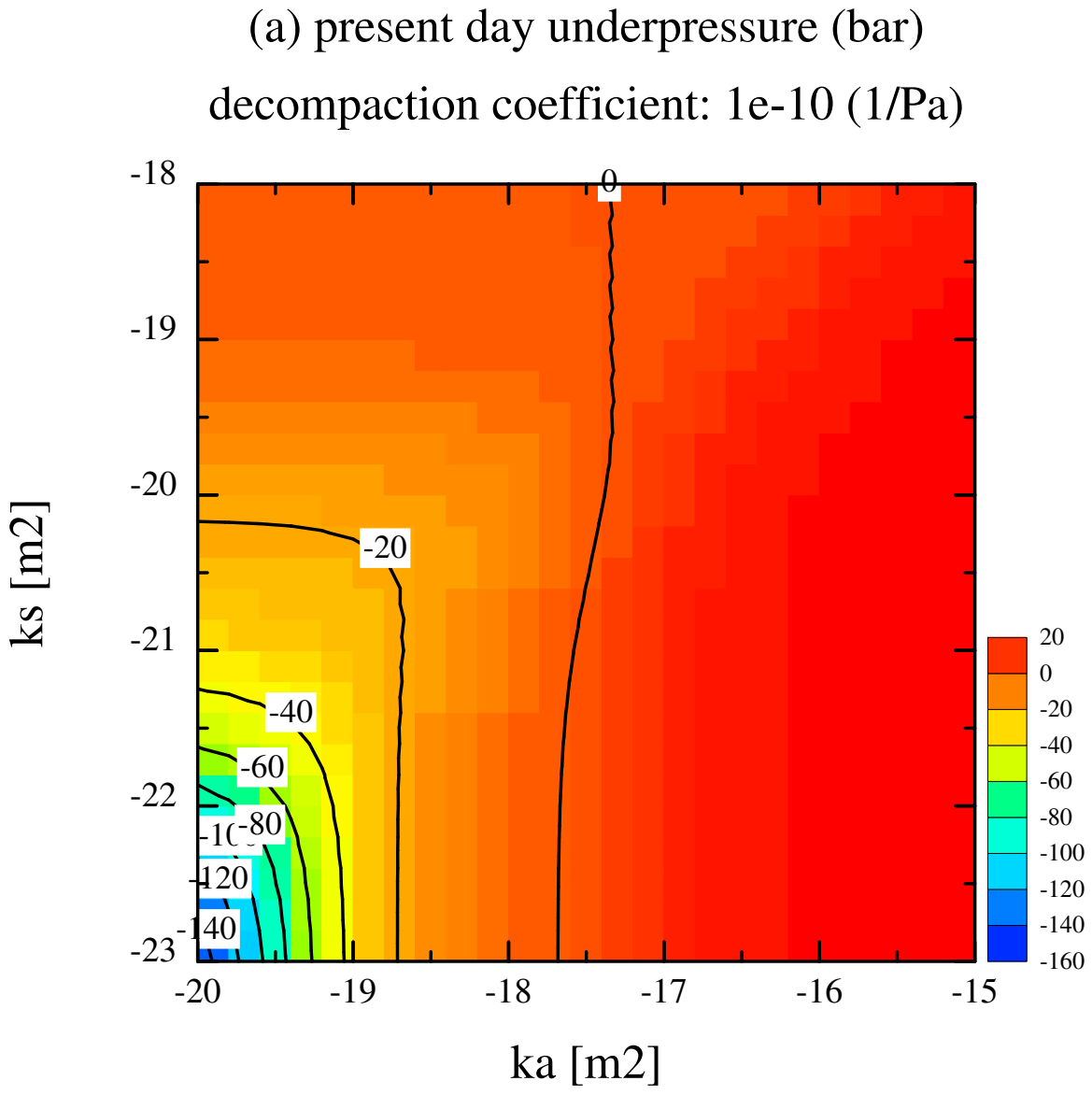
(a) present day underpressure (bar)
decompaction coefficient: 1e-10 (1/Pa)
ks [m2]
ka [m2]
-18
-19
-20
-21
-22
-23
-20
-19
-18
-17
-16
-15
0
-20
-40
-60
-80
-120
-140
20
0
-20
-40
-60
-80
-100
-120
-140
-160

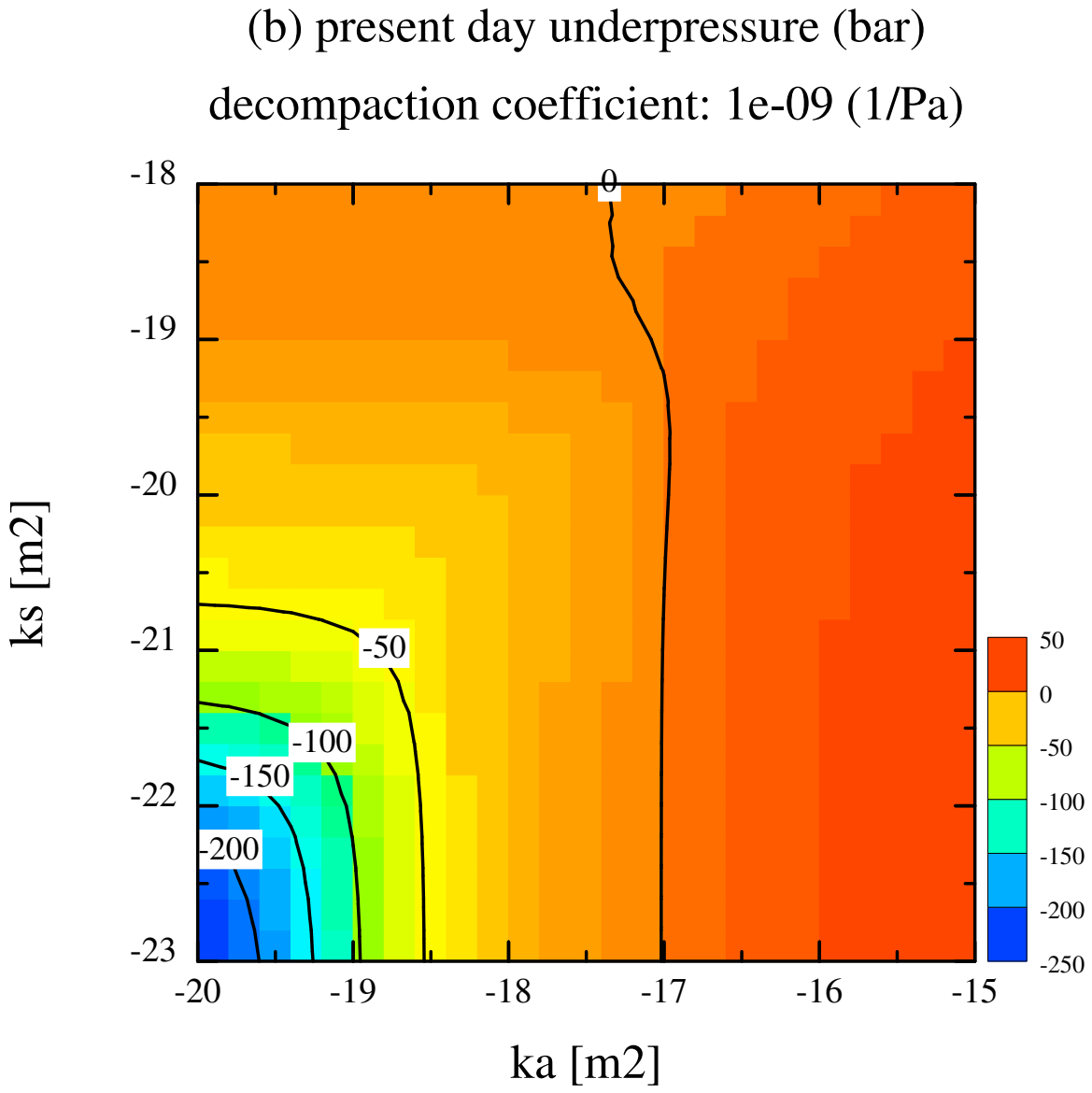
(b) present day underpressure (bar)
decompaction coefficient: 1e-09 (1/Pa)
ks [m2]
ka [m2]
-18
-19
-20
-21
-22
-23
-20
-19
-18
-17
-16
-15
0
-50
-100
-150
-200
50
0
-50
-100
-150
-200
-250

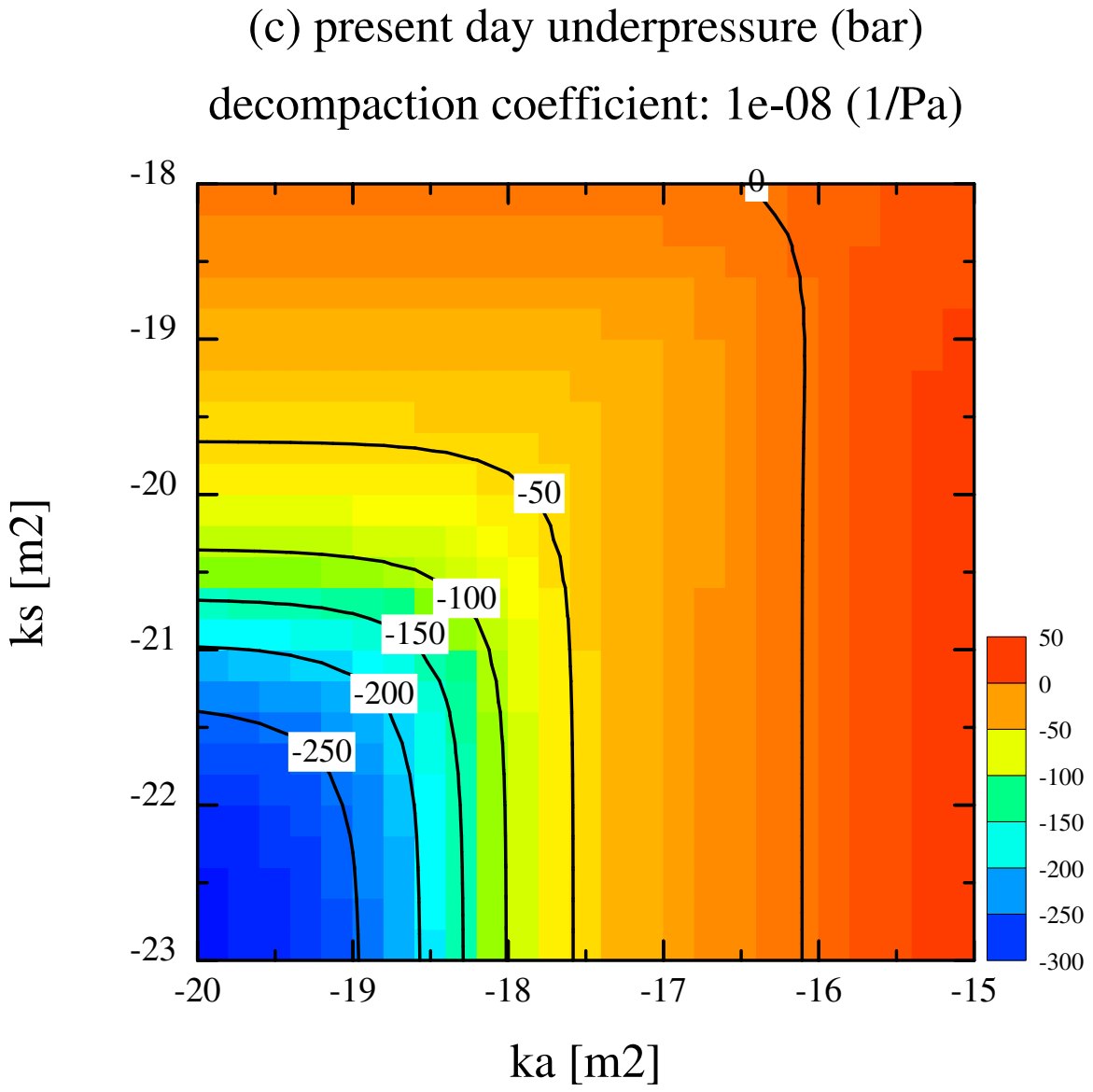
(c) present day underpressure (bar)
decompaction coefficient: 1e-08 (1/Pa)
ks [m2]
ka [m2]
-18
-19
-20
-21
-22
-23
-20
-19
-18
-17
-16
-15
0
-50
-100
-150
-200
-250
50
0
-50
-100
-150
-200
-250
-300

(a)

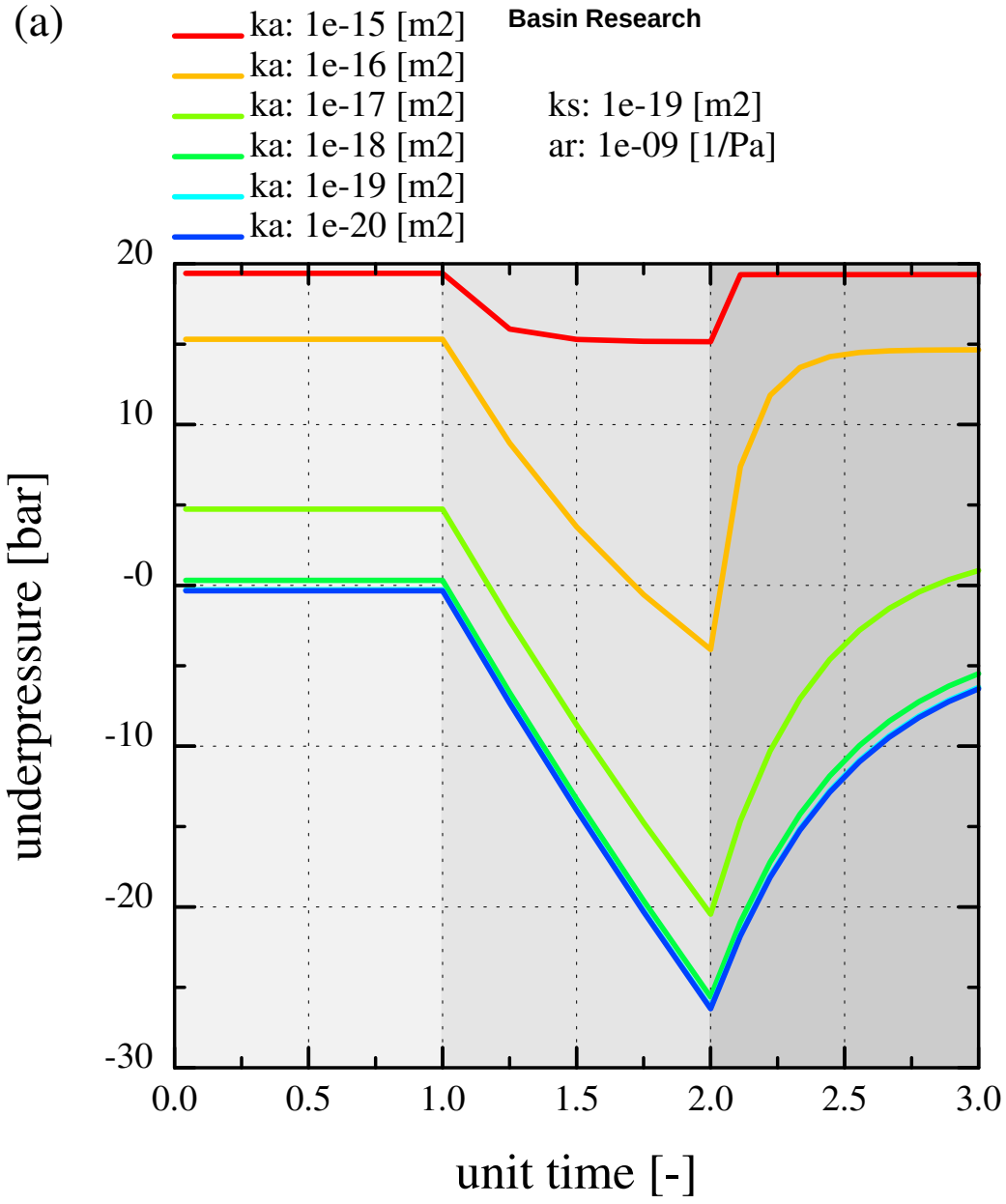
ka: 1e-15 [m2]
ka: 1e-16 [m2]
ka: 1e-17 [m2]
ka: 1e-18 [m2]
ka: 1e-19 [m2]
ka: 1e-20 [m2]
ks: 1e-19 [m2]
ar: 1e-09 [1/Pa]
underpressure [bar]
20
10
-0
-10
-20
-30
0.0
0.5
1.0
1.5
2.0
2.5
3.0
unit time [-]

(b)



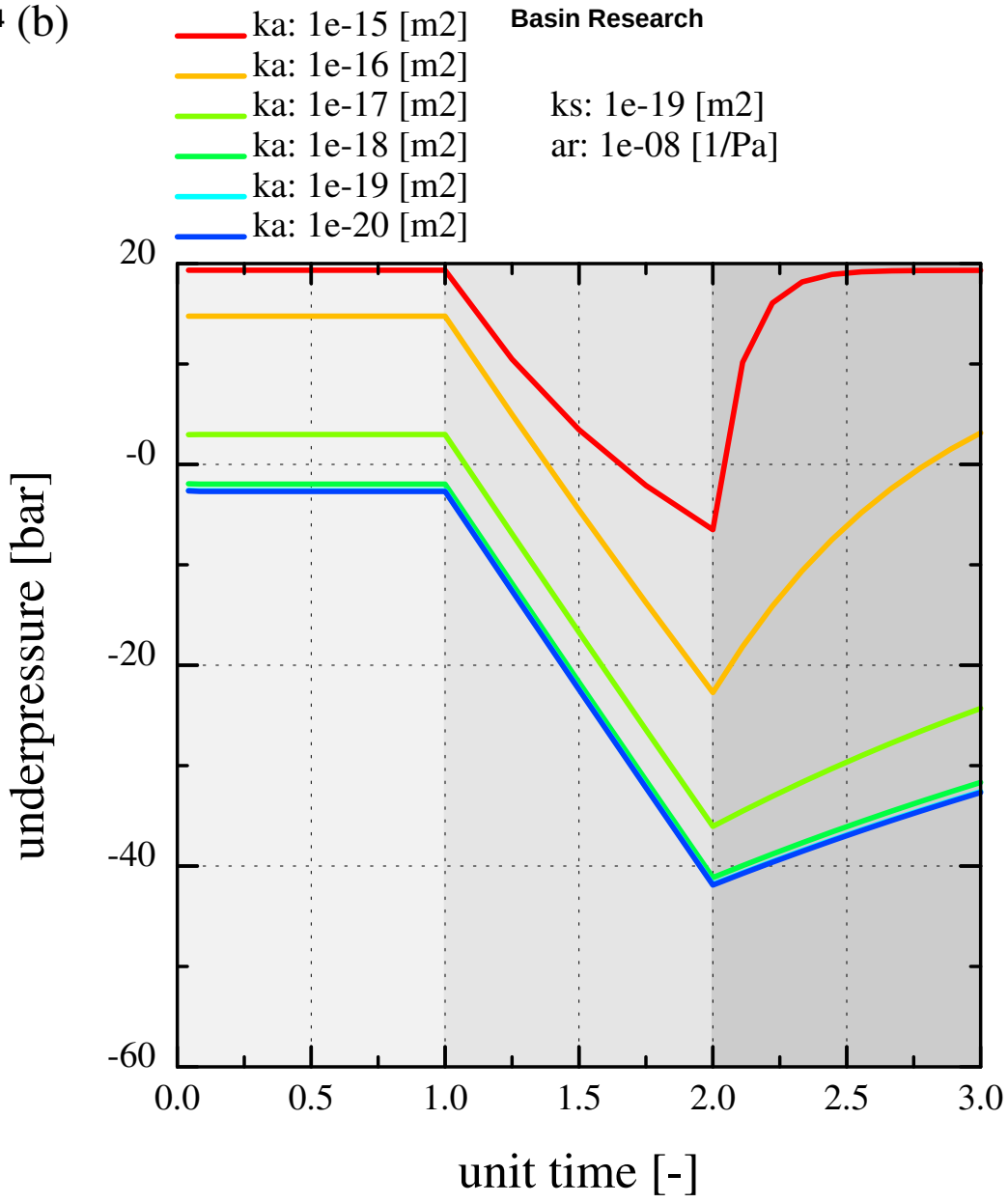
ka: 1e-15 [m2]
ka: 1e-16 [m2]
ka: 1e-17 [m2]
ka: 1e-18 [m2]
ka: 1e-19 [m2]
ka: 1e-20 [m2]
ks: 1e-19 [m2]
ar: 1e-08 [1/Pa]
underpressure [bar]
20
-0
-20
-40
-60
0.0
0.5
1.0
1.5
2.0
2.5
3.0
unit time [-]

(c)

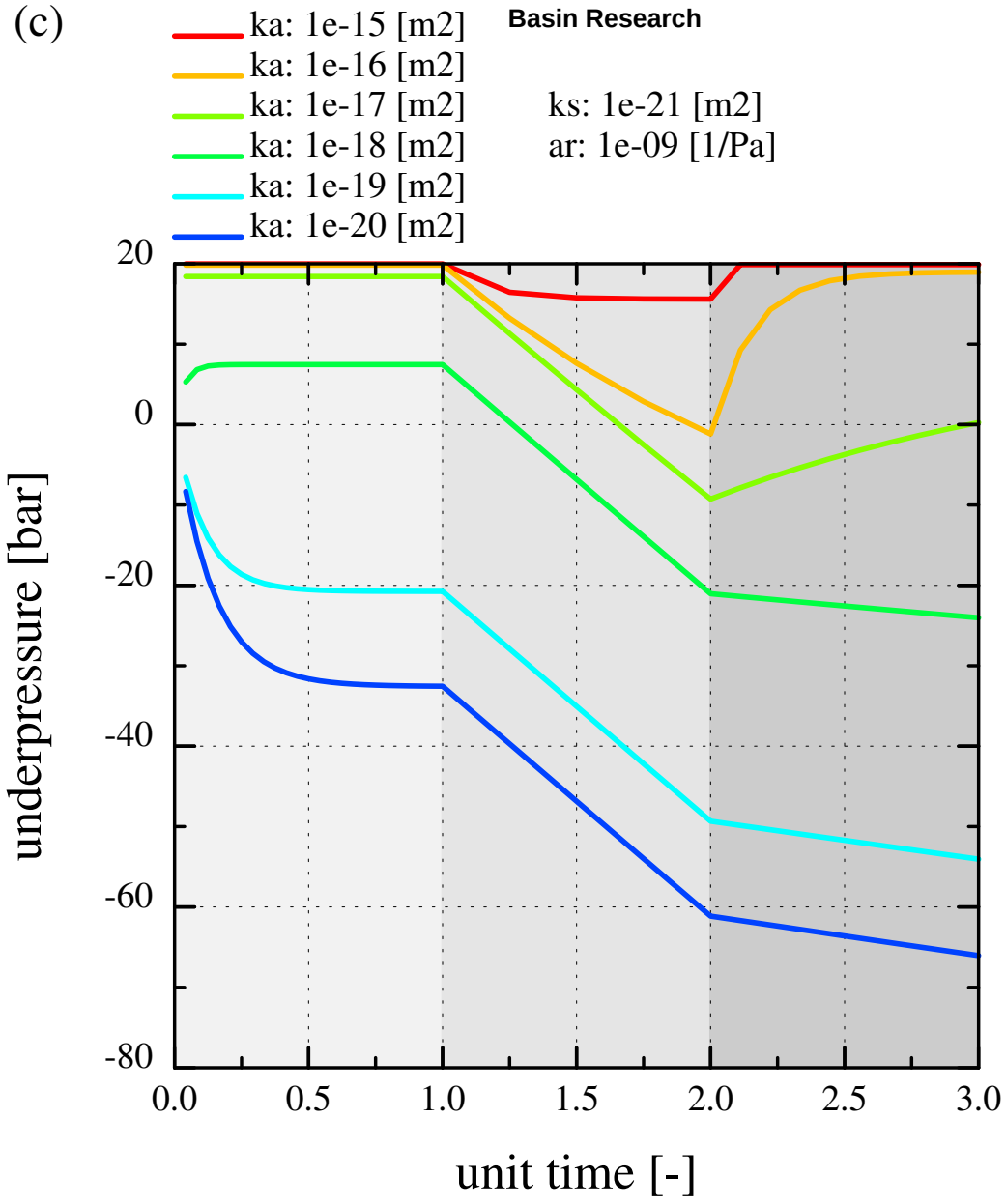
ka: 1e-15 [m2]
ka: 1e-16 [m2]
ka: 1e-17 [m2]
ka: 1e-18 [m2]
ka: 1e-19 [m2]
ka: 1e-20 [m2]
ks: 1e-21 [m2]
ar: 1e-09 [1/Pa]
underpressure [bar]
20
0
-20
-40
-60
-80
0.0
0.5
1.0
1.5
2.0
2.5
3.0
unit time [-]

(d)



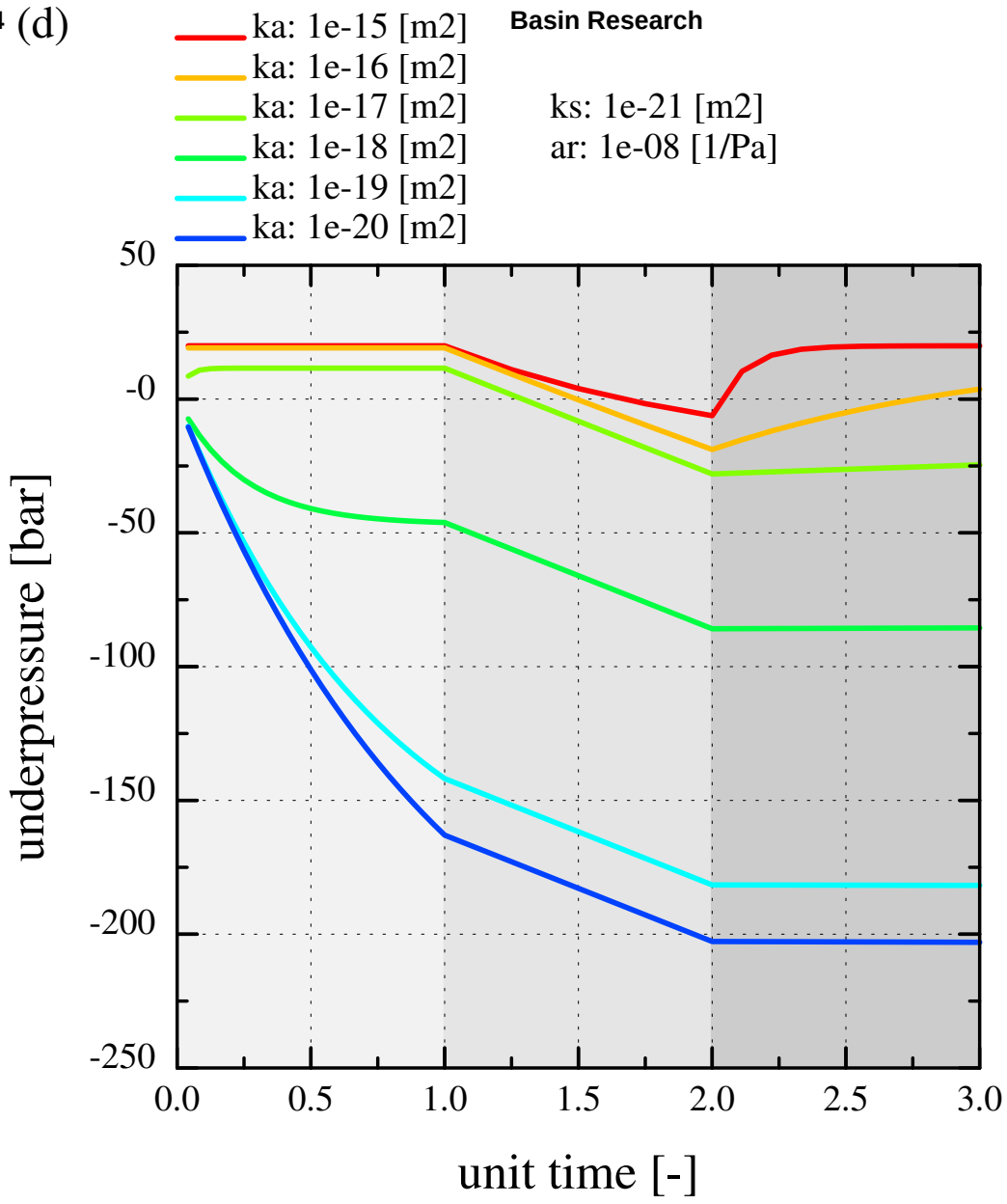
ka: 1e-15 [m2]
ka: 1e-16 [m2]
ka: 1e-17 [m2]
ka: 1e-18 [m2]
ka: 1e-19 [m2]
ka: 1e-20 [m2]
ks: 1e-21 [m2]
ar: 1e-08 [1/Pa]
underpressure [bar]
50
-0
-50
-100
-150
-200
-250
0.0
0.5
1.0
1.5
2.0
2.5
3.0
unit time [-]

(a)

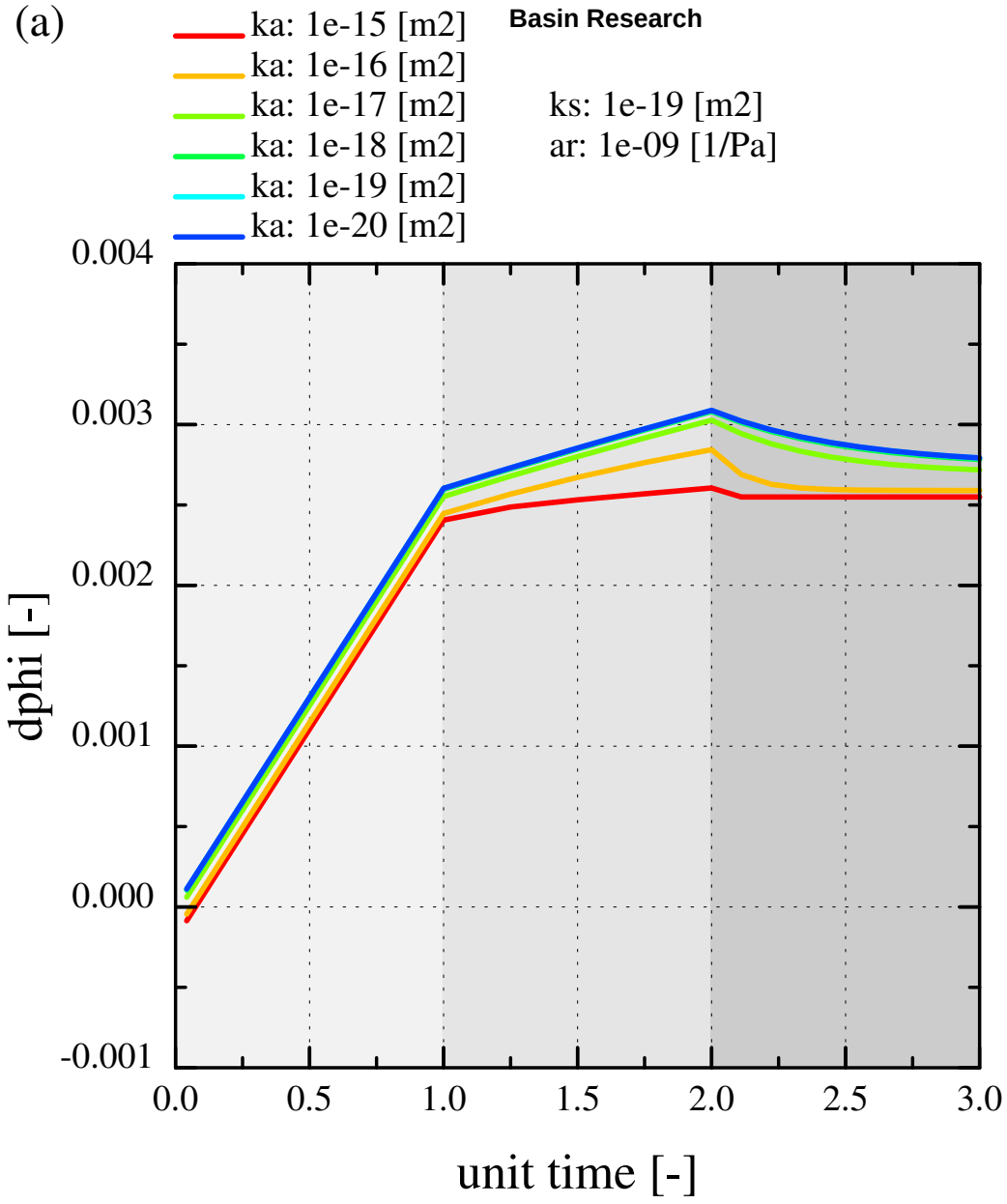
ka: 1e-15 [m2]
ka: 1e-16 [m2]
ka: 1e-17 [m2]
ka: 1e-18 [m2]
ka: 1e-19 [m2]
ka: 1e-20 [m2]
ks: 1e-19 [m2]
ar: 1e-09 [1/Pa]
0.004
0.003
0.002
0.001
0.000
-0.001
dphi [-]
0.0
0.5
1.0
1.5
2.0
2.5
3.0
unit time [-]

(b)



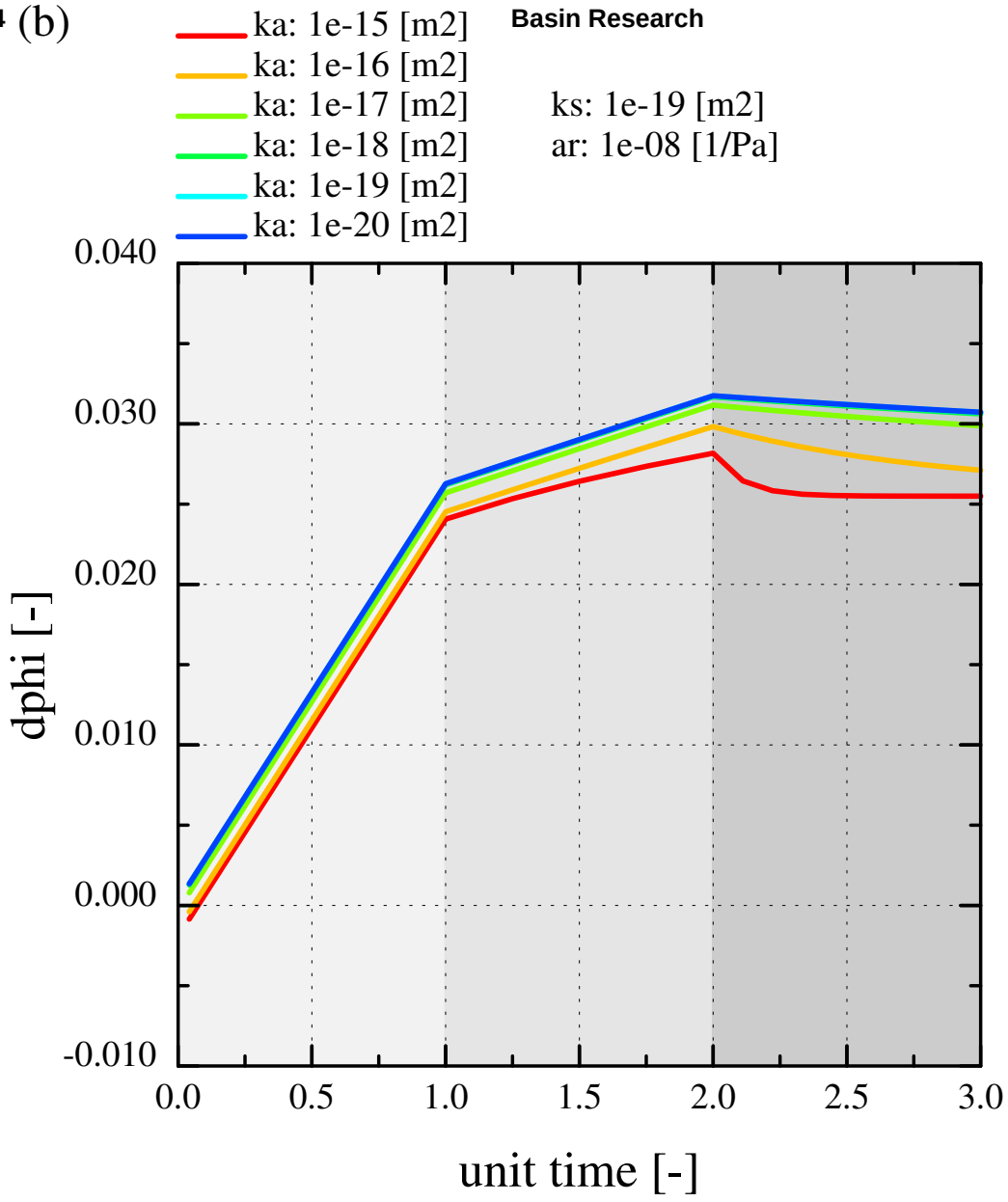
ka: 1e-15 [m2]
ka: 1e-16 [m2]
ka: 1e-17 [m2]
ka: 1e-18 [m2]
ka: 1e-19 [m2]
ka: 1e-20 [m2]
ks: 1e-19 [m2]
ar: 1e-08 [1/Pa]
0.040
0.030
0.020
0.010
0.000
-0.010
dphi [-]
0.0
0.5
1.0
1.5
2.0
2.5
3.0
unit time [-]

(c)

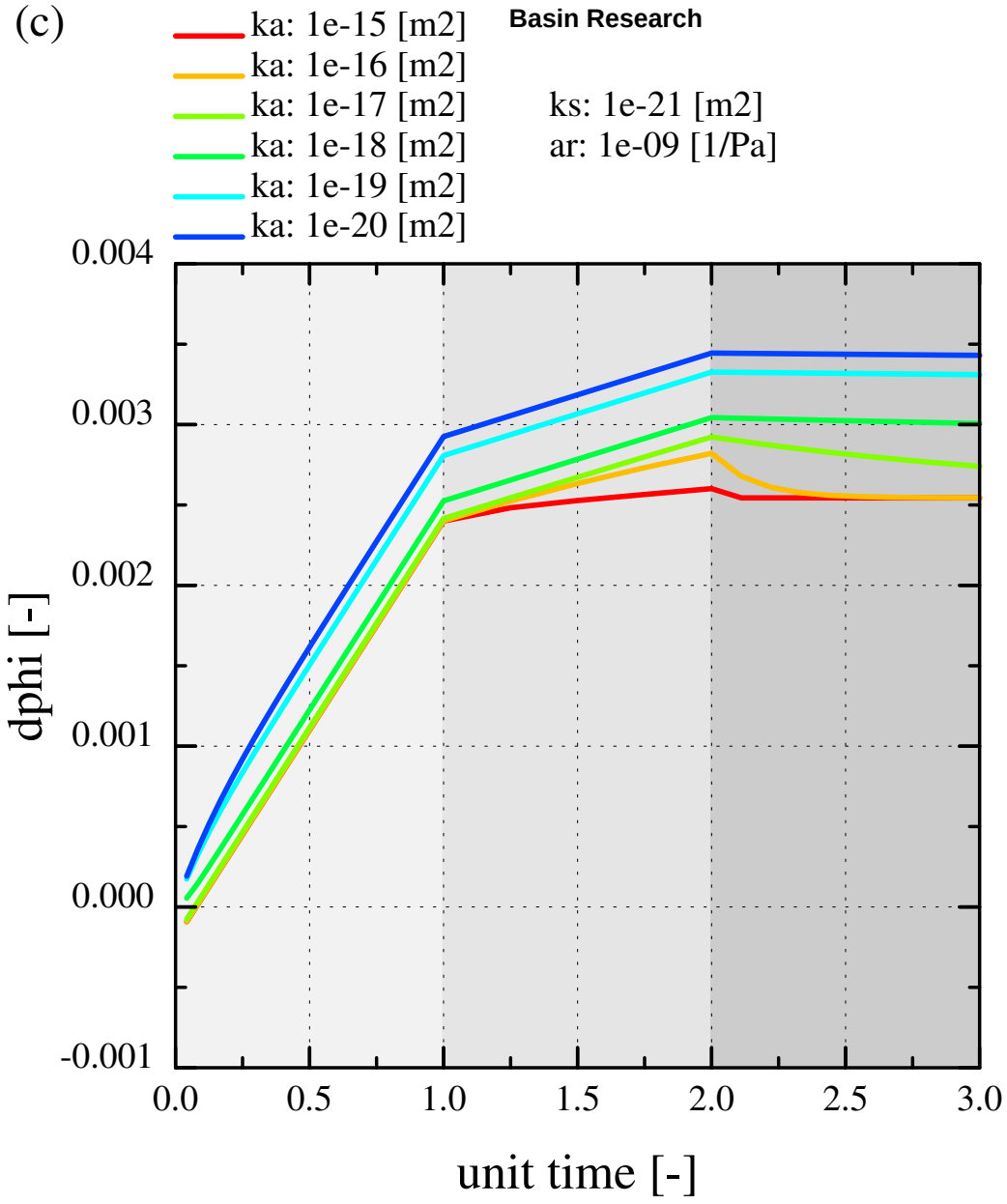
ka: 1e-15 [m2]
ka: 1e-16 [m2]
ka: 1e-17 [m2]
ka: 1e-18 [m2]
ka: 1e-19 [m2]
ka: 1e-20 [m2]
ks: 1e-21 [m2]
ar: 1e-09 [1/Pa]
0.004
0.003
0.002
0.001
0.000
-0.001
dphi [-]
0.0
0.5
1.0
1.5
2.0
2.5
3.0
unit time [-]

(d)



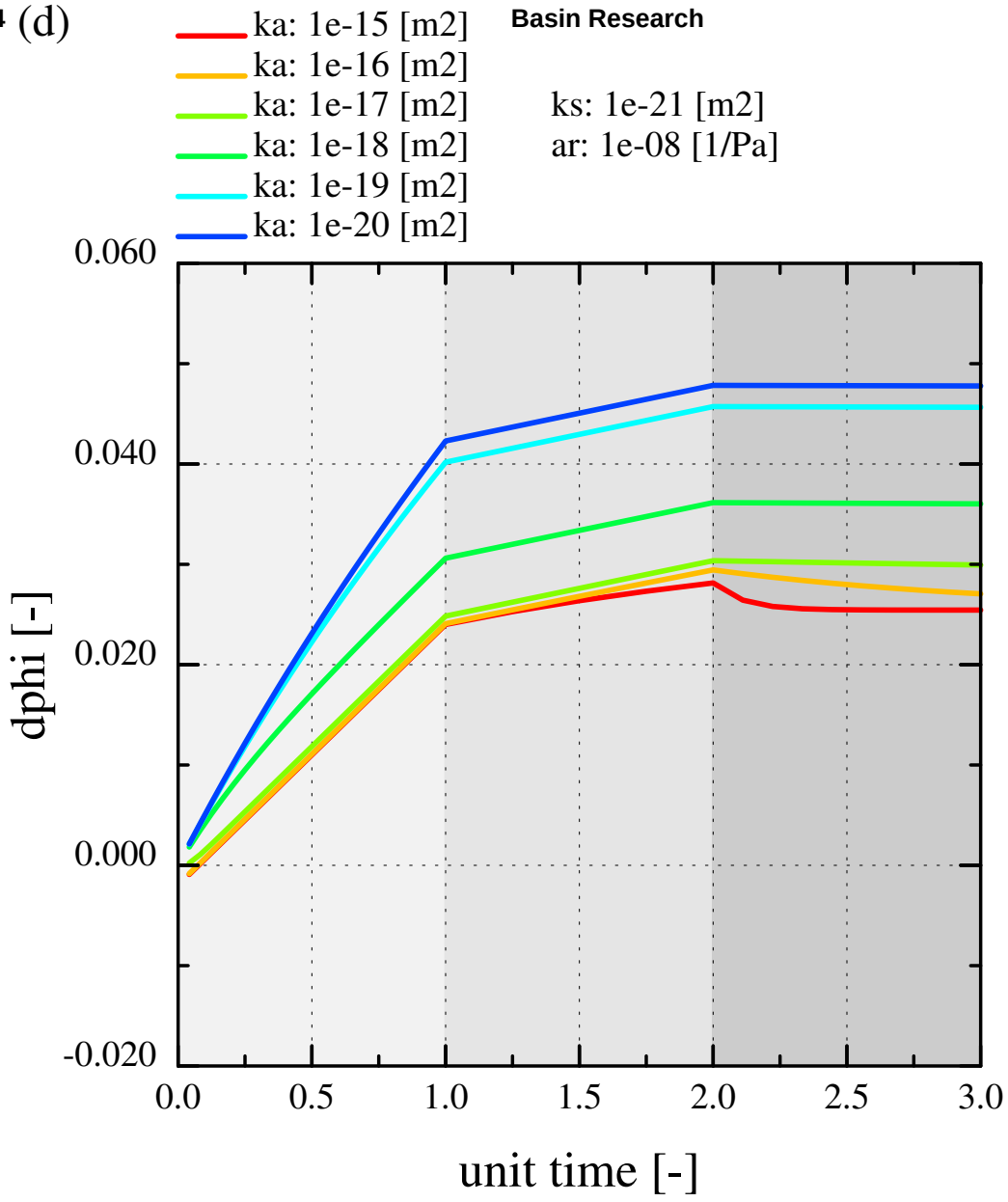

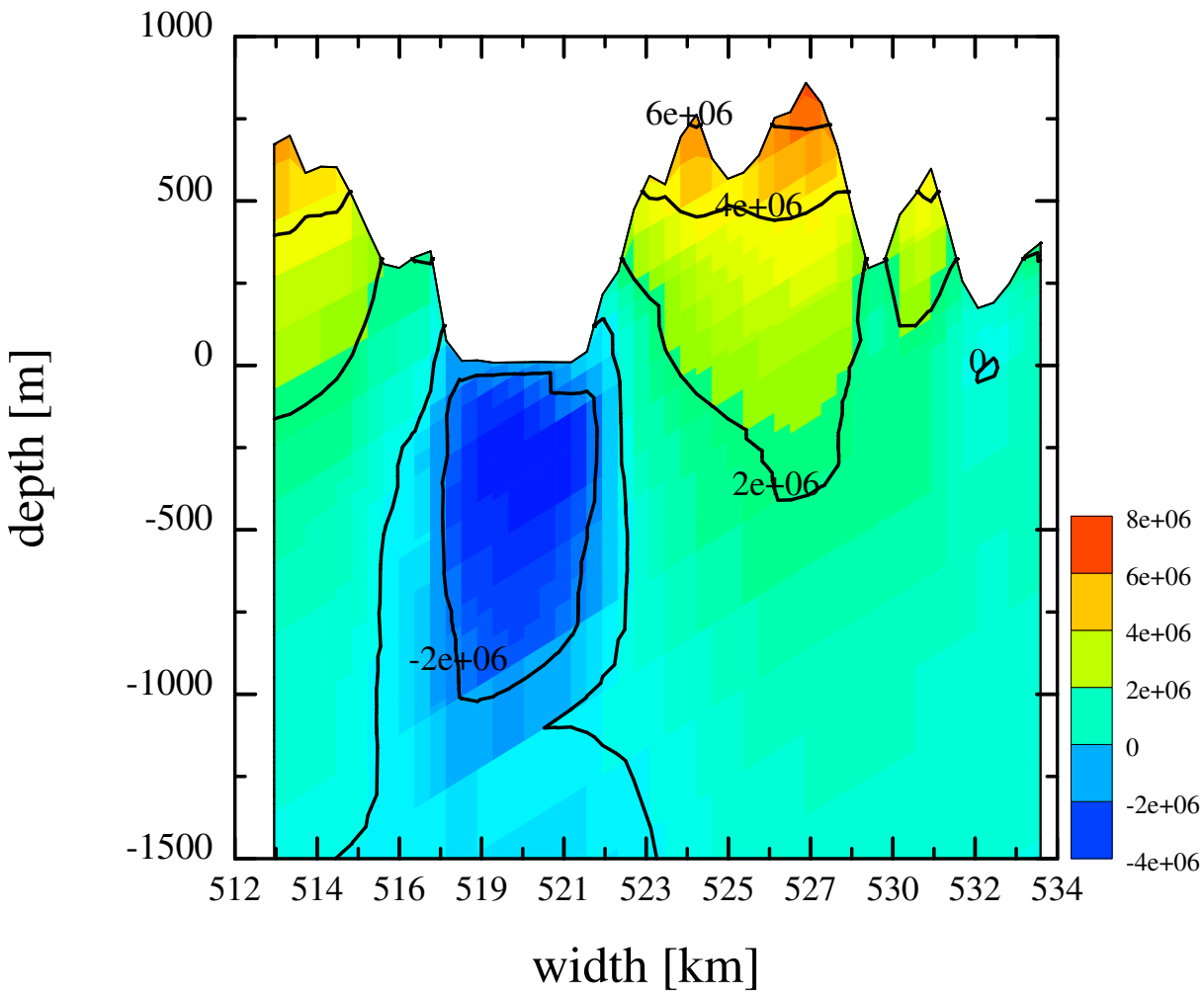
(a) potential [Pa] at time: 0 [Ma]
1000
500
0
-500
-1000
-1500
depth [m]
6e+06
4e+06
2e+06
0
-2e+06
512 514 516 519 521 523 525 527 530 532 534
width [km]
8e+06
6e+06
4e+06
2e+06
0
-2e+06
-4e+06

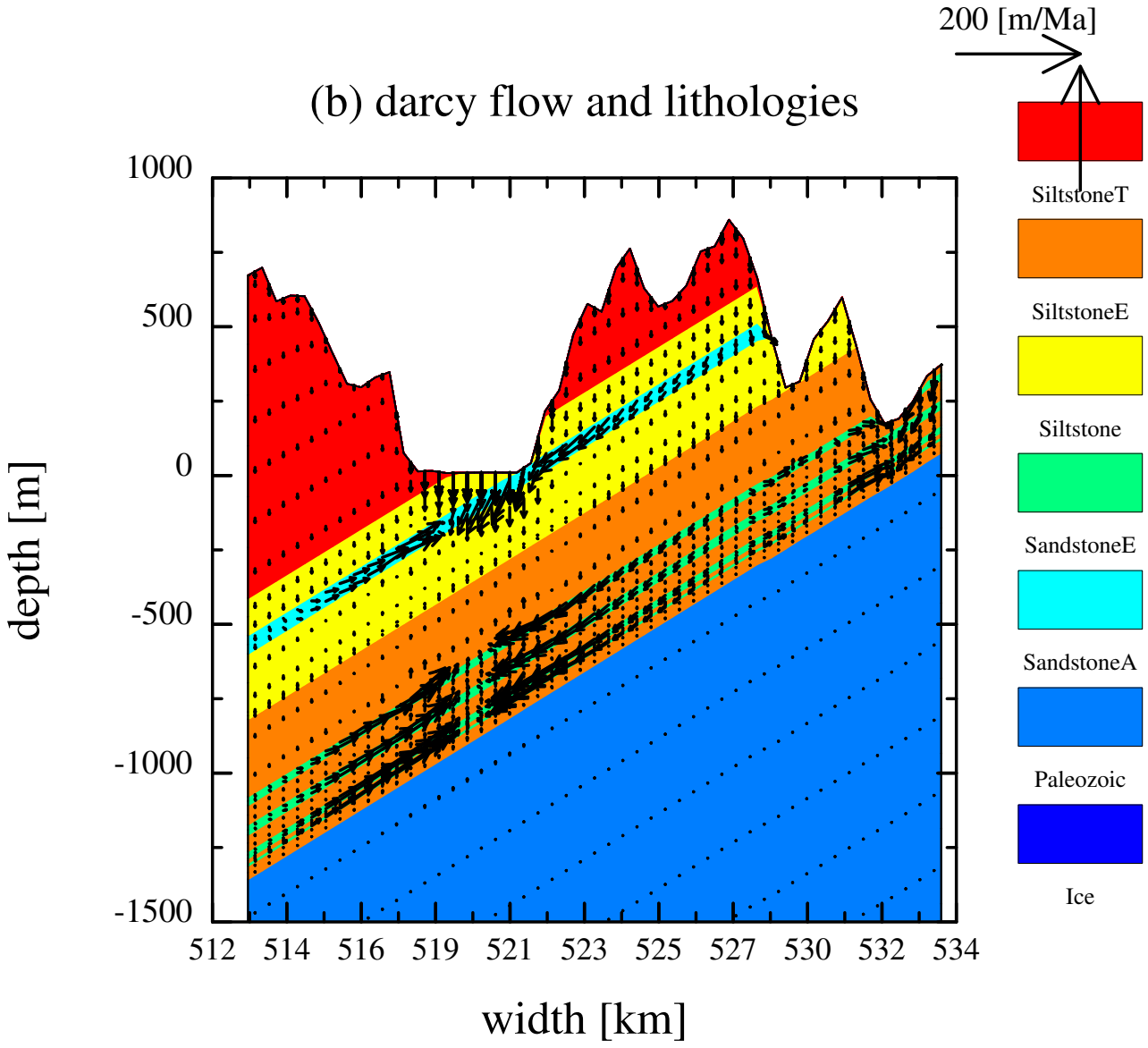
200 [m/Ma]
(b) darcy flow and lithologies
1000
500
0
-500
-1000
-1500
depth [m]
512
514
516
519
521
523
525
527
530
532
534
width [km]
SiltstoneT
SiltstoneE
Siltstone
SandstoneE
SandstoneA
Paleozoic
Ice

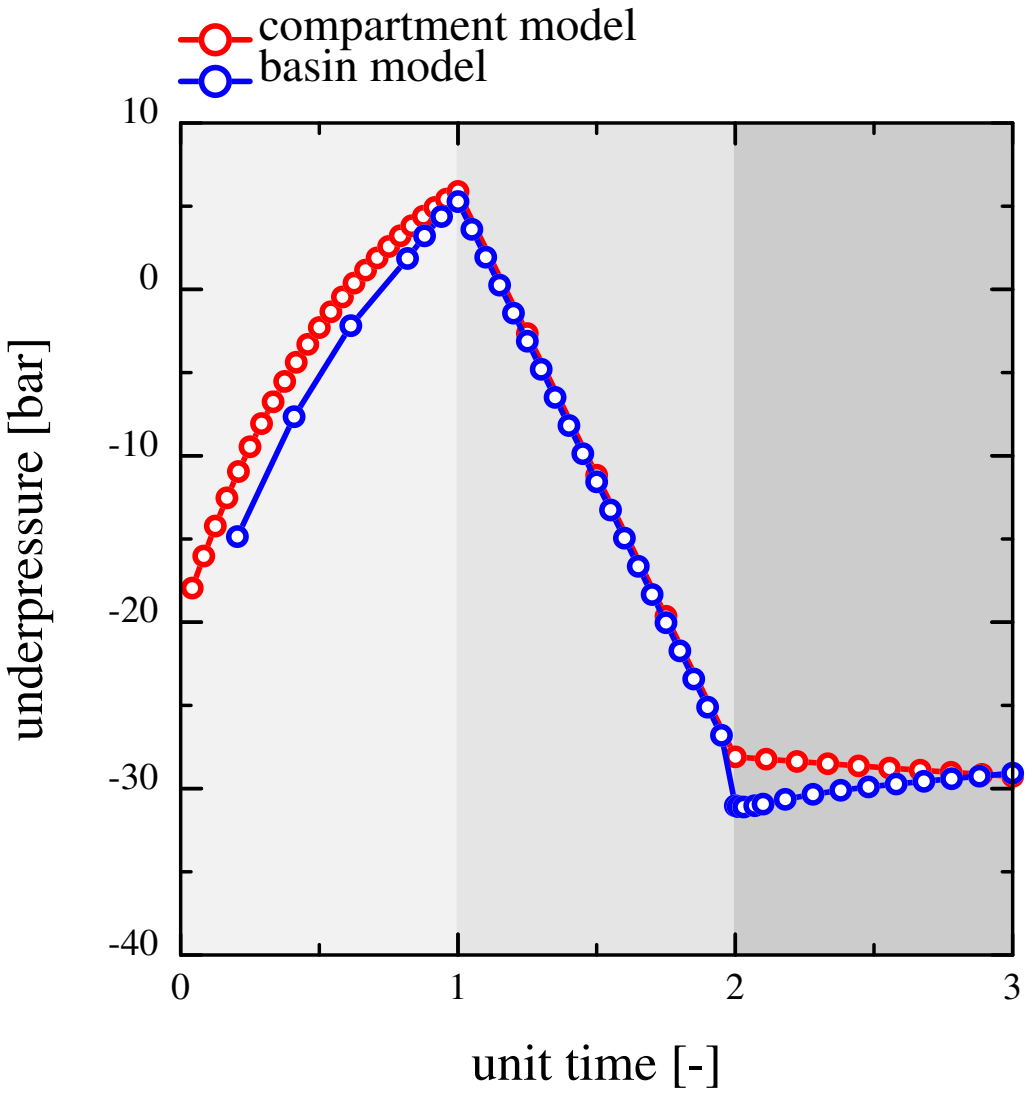
compartment model
basin model
10
0
-10
-20
-30
-40
underpressure [bar]
0
1
2
3
unit time [-]